

Revealing the Shape of Genome Space via K -mer Topology

Yuta Hozumi^{1*} and Guo-Wei Wei^{1,2,3†}

¹ Department of Mathematics,
Michigan State University, East Lansing, MI 48824, USA.

² Department of Electrical and Computer Engineering,
Michigan State University, East Lansing, MI 48824, USA.

³ Department of Biochemistry and Molecular Biology,
Michigan State University, East Lansing, MI 48824, USA.

December 31, 2024

Abstract

Despite decades of effort, understanding the shape of genome space in biology remains a challenge due to the similarity, variability, diversity, and plasticity of evolutionary relationships among species, genes, or other biological entities. We present a k -mer topology method, the first of its kind, to delineate the shape of the genome space. K -mer topology examines the topological persistence and the evolution of the homotopic shape of the sequences of k nucleotides in species, organisms, and genes using persistent Laplacians, a new multiscale combinatorial approach. We also propose a topological genetic distance between species by their topological invariants and non-harmonic spectra over scales. This new metric defines the topological phylogenetic trees of genomes, facilitating species classification and clustering. K -mer topology substantially outperforms state-of-the-art methods on a variety of benchmark datasets, including mammalian mitochondrial genomes, Rhinovirus, SARS-CoV-2 variants, Ebola virus, Hepatitis E virus, Influenza hemagglutinin genes, and whole bacterial genomes. K -mer topology reveals the intrinsic shapes of the genome space and can be directly applied to the rational design of viral vaccines.

keywords: Shape of genome space, Phylogenetic analysis, Topological genetic distance, Persistent Laplacian

*Current address: School of Mathematics, Georgia Institute of Technology, Atlanta, GA 30332

†Corresponding author. Email: weig@msu.edu

Contents

1	Introduction	2
2	Results	3
2.1	Overview of K -mer topology	3
2.2	Genome classification	4
2.3	Phylogenetic analysis	6
2.3.1	Mammalian mitochondrial genomes	6
2.3.2	Rhinovirus	8
2.3.3	SARS-CoV-2 variants	8
2.3.4	Hepatitis E virus	11
2.3.5	Influenza A hemagglutinin genes	11
2.3.6	Ebola virus	11
2.3.7	Bacteria	11
3	Discussion	11
3.1	The shape of genome space from k -mer topology	12
3.2	Genome-specific k -mer distributions	12
3.3	Persistent Laplacian enhancement	12
3.4	High-dimensional topological features	13
3.5	Topological antigenetic distance	13
3.6	Generalizations and applications	13
4	Methods	13
4.1	Persistent homology	13
4.1.1	Simplicial complex	14
4.1.2	Chain complex and homology groups	14
4.1.3	Filtration and persistence	15
4.2	Persistent topological Laplacian	15
4.2.1	Topological Laplacian and its spectrum	15
4.2.2	Filtration and persistence	16
4.3	K -mer topology for nucleotide sequences	16
4.3.1	Position based distance	17
4.3.2	Persistent Laplacian features	18
4.3.3	Topological genetic distance	19
S1	Topological genetic/antigenetic distances	21
S2	Additional classification benchmark	22
S3	Additional materials for phylogenetic analysis using k-mer topology	23
S3.1	Hepatitis E virus genomes	26
S3.2	Influenza A hemagglutinin genes	27
S3.3	Ebola virus	28
S3.4	Bacteria	29
S4	Distribution of k-mers	29
S5	Persistent Laplacian improves persistent homology in phylogenetic analysis	30

S6 Further analysis of persistent Laplacian on DNA sequences	31
S7 Further details on the codes used in comparisons	32
S8 Classification data	32
S9 Phylogenetic analysis data	33

1 Introduction

Phylogenetic analysis of genetic sequences is vital for understanding evolutionary relationships among species and within species [1, 2]. Genetic sequences can be regarded as sequences of letters, that is, four letters for nucleotides and 20 letters for amino acids. Comparison of sequences can be challenging due to nonuniform lengths, mutations, and sequencing and/or assembly errors. In particular, in full-genome comparisons, different species often have dramatically varying lengths, making it challenging to define genetic metrics between sequences. Therefore, having a robust and reliable method to extract meaningful features that encode complex patterns and capture the shape of the genome space is essential and challenging.

Traditional phylogenetic analysis relies on ‘sequence alignment’ using multiple sequence alignment (MSA) tools such as Clustal Omega [3], MAFFT [4], and MUSCLE [5]. Alignment-based methods are effective for identifying mutations in sequences [6–10]. However, these methods may fail when conserved segments are not properly aligned or have different lengths, a common challenge with real-world data. Additionally, alignment-based methods are time-intensive and memory-demanding, making large-scale sequence comparisons difficult. Alternatively, ‘alignment-free methods’ transform variable-length sequences into uniform objects, such as vectors, for sequence analysis [11]. This approach enables the effective comparison of sequences regardless of sequence lengths [12]. Moreover, because alignment-free methods extract features from individual sequences, their computational complexity scales only with the sequence length and the number of sequences [13]. This makes whole-genome comparisons across species more efficient and easily parallelizable [14–17].

Numerous alignment-free methods have been proposed, primarily categorized as word frequency- and information theory-based methods. The former includes k -mer methods [18], where the frequency of words or motifs is counted and concatenated into a vector. Subsequently, the similarity or difference between sequences can be computed using a vector-based distance metric. Several extensions have been proposed to enhance efficiency and distance calculation [16, 19–22]. In information theory-based methods, the distance between sequences is estimated by the amount of shared information between the two sequences using entropy and/ or complexity measures such as Kolmogorov complexity [23], Lempel-Ziv complexity [24], Shannon entropy [25], etc. Comprehensive overviews of these methods can be found in [12, 13, 26]. However, these methods do not incorporate positional information from nucleotides.

Several advanced alignment-free methods have also been proposed. Among them, the natural vector method (NVM) analyzes the moments of the k -mer positions [27, 28]. The chaos game representation (CGR) [29] represents the sequence as an iterative function, which can be visualized as an image [30]. Various generations of CGR have been proposed [31–34]. In addition, other methods such as the discrete Fourier power spectrum method [35, 36], fuzzy integral similarity method [37], and others [38] have been developed for phylogenetic analysis.

Persistent homology is an algebraic topology tool for analyzing the shape of complex data [39]. Chan et al. [40] utilized persistent homology to compute sequence dissimilarity in viruses. The 0th-order homology and the 1st-order homology corresponded to vertical and horizontal evolution, respectively. This approach was used in analyzing the evolution of SARS-CoV-2 through the topological recurrence index (tRI) [9]. Nguyen et al. [41] applied persistent homology to the CGR of viral sequences. However, persistent homology neglects the intrinsic biological characteristics of genetic sequences. To overcome the limitation of persistent homology, persistent topological Laplacians (PTLs), including persistent combinatorial Laplacian or persistent spectral graph for point cloud data [42] and persistent Hodge Laplacian for data on manifolds [43] were introduced. By tracking the changes in the harmonic and non-harmonic spectra of a series of PTLs induced by filtration, one can uncover the topological and geometrical shape of the data. Specifically, the multiplicity of the harmonic spectra, i.e., the zero-eigenvalues, gives the Betti number of persistent homology at appropriate topological dimensions, while the non-harmonic spectra reveal the homotopic shape evolution.

In this work, we introduce the k -mer topology, a novel topological approach for sequence analysis. K -mer

topology extracts the topological persistence of k -mer segments in a genome through persistent homology and/ or persistent Laplacian, the latter further captures the evolution of the homotopic shape of k -mers during filtration. We also define a novel topological genetic distance to define phylogenetic trees and position individual species, organisms, or genes in the genome space. To benchmark the proposed method, we consider both classification tasks and phylogenetic analysis. Our method significantly outperforms other competing methods in viral classification and whole-genome phylogenetic analysis. The proposed topological genetic distance not only sheds light on genome evolution, but also provides a reliable antigenetic distance for the rational design of viral vaccines.

2 Results

2.1 Overview of K -mer topology

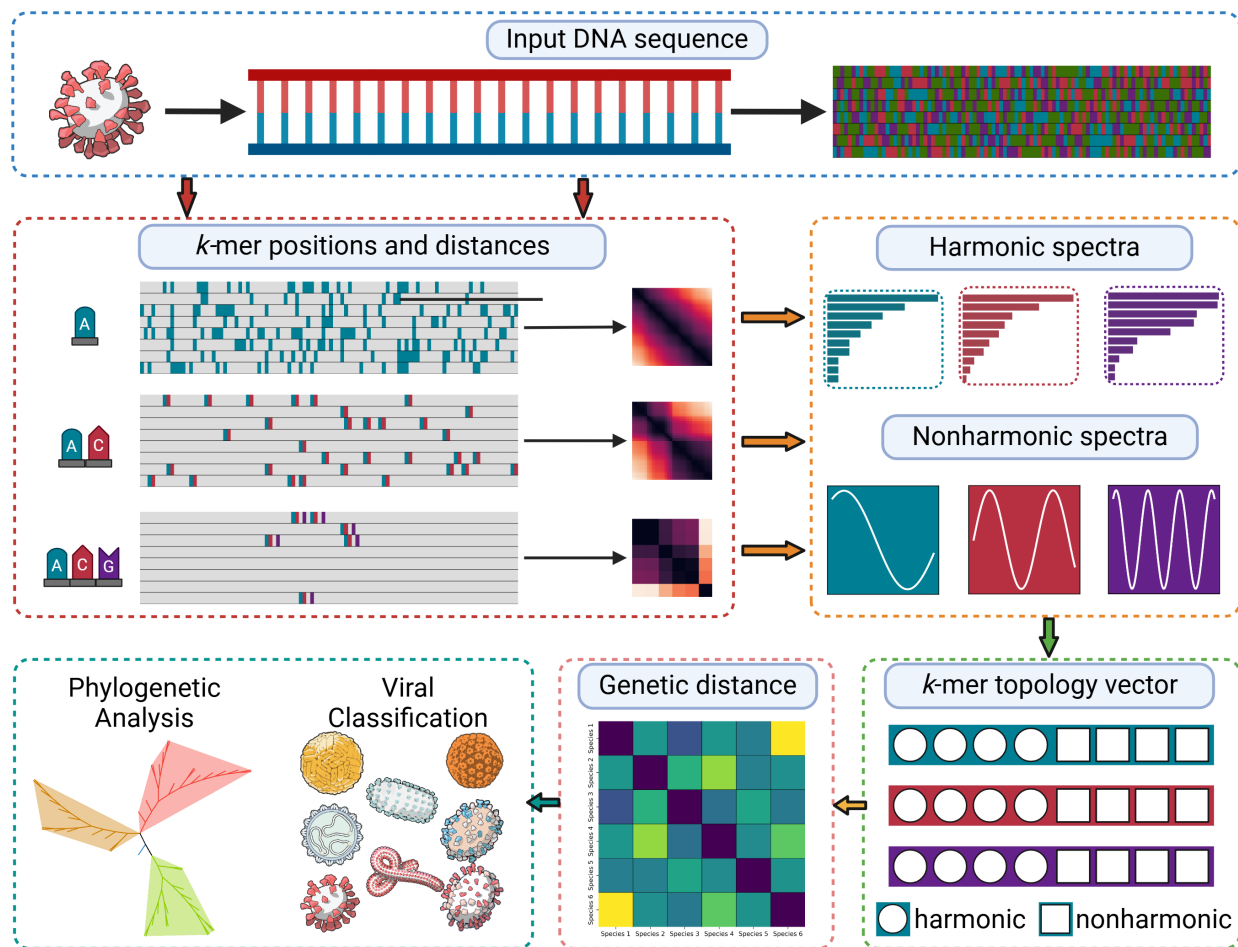


Figure 1: Workflow of k -mer topology. From a query sequence, k -mers are extracted. The positions of individual k -mers are used to compute the k -mer specific distances. Using these distances, persistent Laplacian computes the persistent spectra of k -mers. The harmonic persistent spectrum of the persistent Laplacian provides the persistent Betti numbers, which represent the number of connected k -mer components across multiple scales, while the non-harmonic persistent spectrum yields the homotopic shape evolution of the k -mers over scales. These features are converted into a genome topological vector. Topological genetic distances are defined between genome topological vectors for genome classification and/or phylogenetic analysis.

The workflow of the k -mer topology is depicted in Figure 1¹. Starting with a given sequence, the positions of the k -mers are extracted. For each set of k -mers, the pairwise distances between its positions are calculated, resulting in k -mer-specific distances. Using these k -mer-specific distances, a family of persistent Laplacian spectra is computed according to filtration. The kernels of persistent Laplacians give rise to harmonic persistent spectra which contain the same topological invariants as persistent homology does. The non-harmonic persistent spectra, namely the non-zero eigenvalues, capture additional shape information of the k -mers across multiple scales. These features are used to construct a k -mer-specific topological vector for each sequence. Topological genetic distances between the sequence vectors are defined and used for genome classification and phylogenetic analysis. More details of the proposed k -mer topology are provided in section 4.

2.2 Genome classification

We first validate k -mer topology on a viral classification problem using reference sequences collected from the NCBI Virus Database. The viral families served as classification labels. Additionally, the labels in the NCBI Virus Database evolve because the International Committee on Taxonomy of Viruses (ICTV) continuously updates them based on new research findings, indicating the challenge of the problem. A summary of recent changes is given in Table S3. Therefore, it is crucial for viral classification methods to remain robust to these updates.

For the classification task, we followed the methodology described by Sun et al. [44]. A 1-nearest neighbor (1-NN) classification was performed on the distance matrix generated from the k -mer topology. Specifically, for a given sequence, if the closest sequence according to our metric belongs to the same viral family, the classification is considered correct. This approach simulates real-world applications, where for a query sequence, the most similar sequence is identified and can be further analyzed in detail.

Additionally, we performed 5-nearest neighbor (5-NN) classification on the same dataset to verify that our method can also detect similar sequences. Since some families contained a small number of samples, we excluded all families with fewer than 15 sequences. We then applied 5-fold cross-validation with 30 random seeds to obtain the 5-NN classification results.

¹Illustration from NIAID NIH BIOART Source #64, 144, 155, 156, 187, 391, 464, 545. Accessed by [https://bioart.niaid.nih.gov/bioart/***](https://bioart.niaid.nih.gov/bioart/***, where *** is the #), where *** is the #.

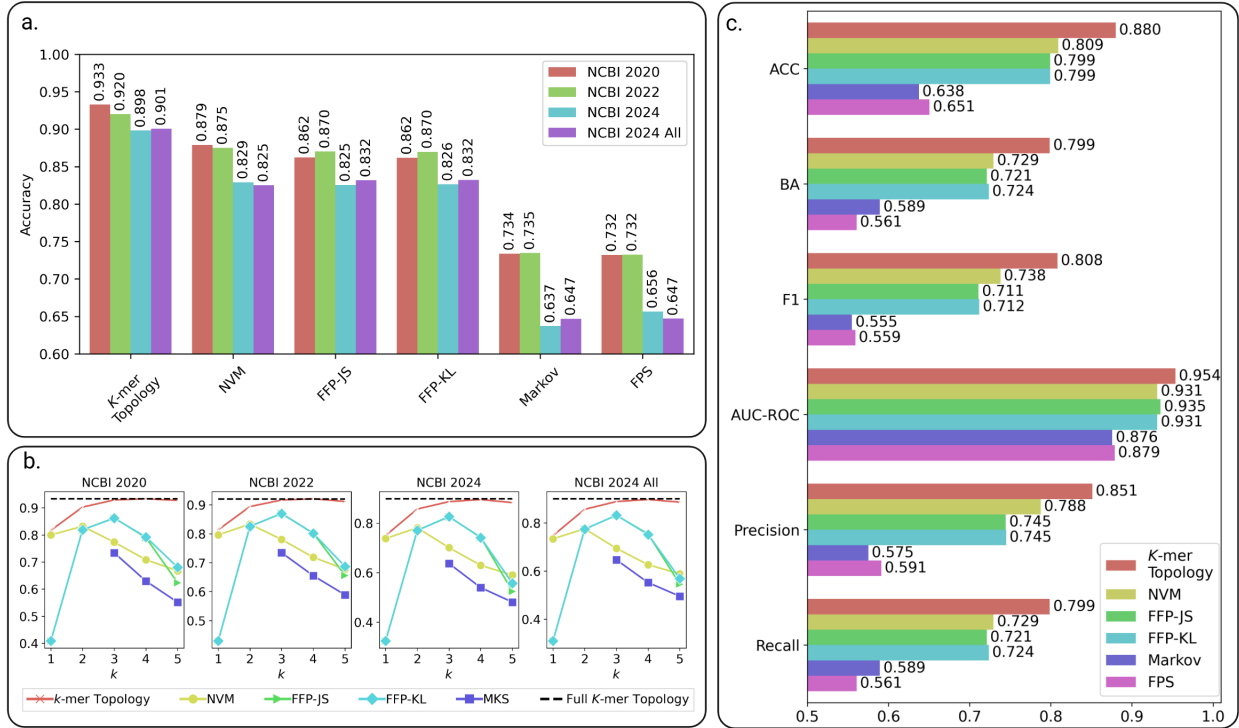


Figure 2: Benchmark of k -mer topology on NCBI viral reference sequences from 2020, 2022, and 2024. The NCBI 2024 All dataset includes sequences with invalid nucleotides as well as sequences assigned to unranked families. (a) Accuracy comparison of our method against the Natural Vector Method (NVM) [44], Jensen-Shannon divergence (FFP-JS) [16, 45], Kullback–Leibler divergence (FFP-KL) [26], Markov K-String (Markov) [46], and Fourier Power Spectrum (FPS) methods [35]. (b) Classification accuracy for each k from $k = 1$ to $k = 5$. The black dotted line indicates the accuracy of the weighted sum of k -mer topologies. The Markov K-String method starts from $k = 3$ because it requires $k - 1$ -mers and $k - 2$ -mers to compute features for a given k . (c) 5-NN classification performance on the NCBI 2024 dataset, including all sequences. Stratified 5-fold cross-validation was performed using 30 random seeds. The bars represent the average scores for each method. Metrics including accuracy (ACC), balanced accuracy (BA), macro-F1 (F1), area under the receiver operating characteristic curve (AUC-ROC), recall, and precision were computed for each method.

Figure 2 compares k -mer topology with the Natural Vector Method (NVM) [44], Jensen-Shannon Divergence (FFP-JS) [16, 45], Kullback-Leibler Divergence (FFP-KL) [26], Markov K-String (Markov) [46], and Fourier Power Spectrum (FPS) [35]. FFP-JS and FFP-KL are information theory-based methods that compute sequence dissimilarity by analyzing feature frequency profiles (FFPs), which are normalized k -mer counts. The Markov K-String method predicts the expected frequency of k -mers using a Markov model and compares it with the observed k -mer frequencies. FPS converts sequences into signals, applies a Fourier transform, and uses statistics derived from the Fourier coefficients as features.

The upper row of Figure 2 shows the classification accuracy for each dataset using the parameters specified in the original work. For k -mer topology, $k = 5$ was used, while for FFP-JS and FFP-KL, $k = 3$ was selected. The bottom row displays the classification accuracy as a function of varying k -mer sizes, with the dashed black line representing the accuracy achieved by the weighted sum of different k -mer sizes.

Figure 2 (a) presents the 1-NN classification accuracy in all four datasets. Our method consistently outperforms all other methods in all datasets. In particular, the accuracy of the k -mer topology in the NCBI 2024 All and NCBI 2024 datasets is comparable. Although NCBI 2024 excludes sequences with invalid nucleotides and unranked families, NCBI 2024 All includes sequences with these anomalies, highlighting the robustness of our method in handling real-world scenarios where sequence errors are common.

A general decrease in accuracy from 2020 to 2024 is observed in all methods. This decline can be attributed to changes in viral classification, such as the abolition of large families like Reoviridae in 2020, resulting in its members being redistributed into smaller families. As a result, the NCBI 2024 dataset poses greater classification challenges compared to the NCBI 2020 dataset.

The superior performance of the k -mer topology in the NCBI 2024 dataset demonstrates its ability not only to accurately classify viral families but also to effectively distinguish between closely related sequences within each family.

Furthermore, we evaluated the impact of varying the k values, as shown in Figure 2 (b). In individual k -mer analysis, the k -mer topology consistently outperformed all other methods by a significant margin. Interestingly, our method exhibited improved accuracy as k increased, while other methods showed a decrease in accuracy after $k = 3$. This trend aligns with the biological encoding of amino acids through nucleotide triplets (codons), suggesting that $k = 3$ may provide the most informative features for viral classification.

Figure 2 (c) presents the 5-NN classification results on the NCBI 2020 All dataset, with comparisons for the other three datasets detailed in Section S2 of the supplementary materials. Our method achieved superior performance across all metrics, including accuracy (ACC), balanced accuracy (BA), macro F1 score (F1), macro area under the receiver operating characteristic curve (AUC-ROC), recall, and precision for all four datasets. Macro scores were used to ensure equal contribution from all viral families. For AUC-ROC, we used the one-versus-rest approach, where each family was compared against all the others. The outstanding performance of k -mer topology in both 1-NN and 5-NN classification tasks demonstrates its robustness in identifying sequences similar to the queried sequence.

2.3 Phylogenetic analysis

In order to further validate our method, we consider phylogenetic analysis of 7 benchmark problems. Figures S2 and S3 summarize the phylogenetic analysis of the k -mer topology. Further details of the comparative analysis can be found in the subsequent sections and in section S3 of the supporting materials. Essentially, the k -mer topology provides a completely correct phylogenetic analysis of all problems. Comparisons with state-of-the-art methods, such as NVM [44], FFP-JS [16, 45], FFP-KL [26], Markov [20], and FPS [35], are described below.

2.3.1 Mammalian mitochondrial genomes

Figure 3 shows the comparison of six methods for the phylogenetic tree analysis of 42 complete mitochondrial genomes. The mitochondrial genomes are classified according to the host species' classification, which includes Artiodactyla, Carnivora, Cetacea, Erinaceomorpha, Lagomorpha, Perissodactyla, Primates, and Rodentia. Our k -mer topology successfully clusters all genomes into their respective clades. NVM, FPS-JS, FPS-KL, and Markov all separate Carnivora mitochondrial genomes into multiple clades. NVM, Markov, and FPS have misclassified Artiodactyla mitochondrial genomes.

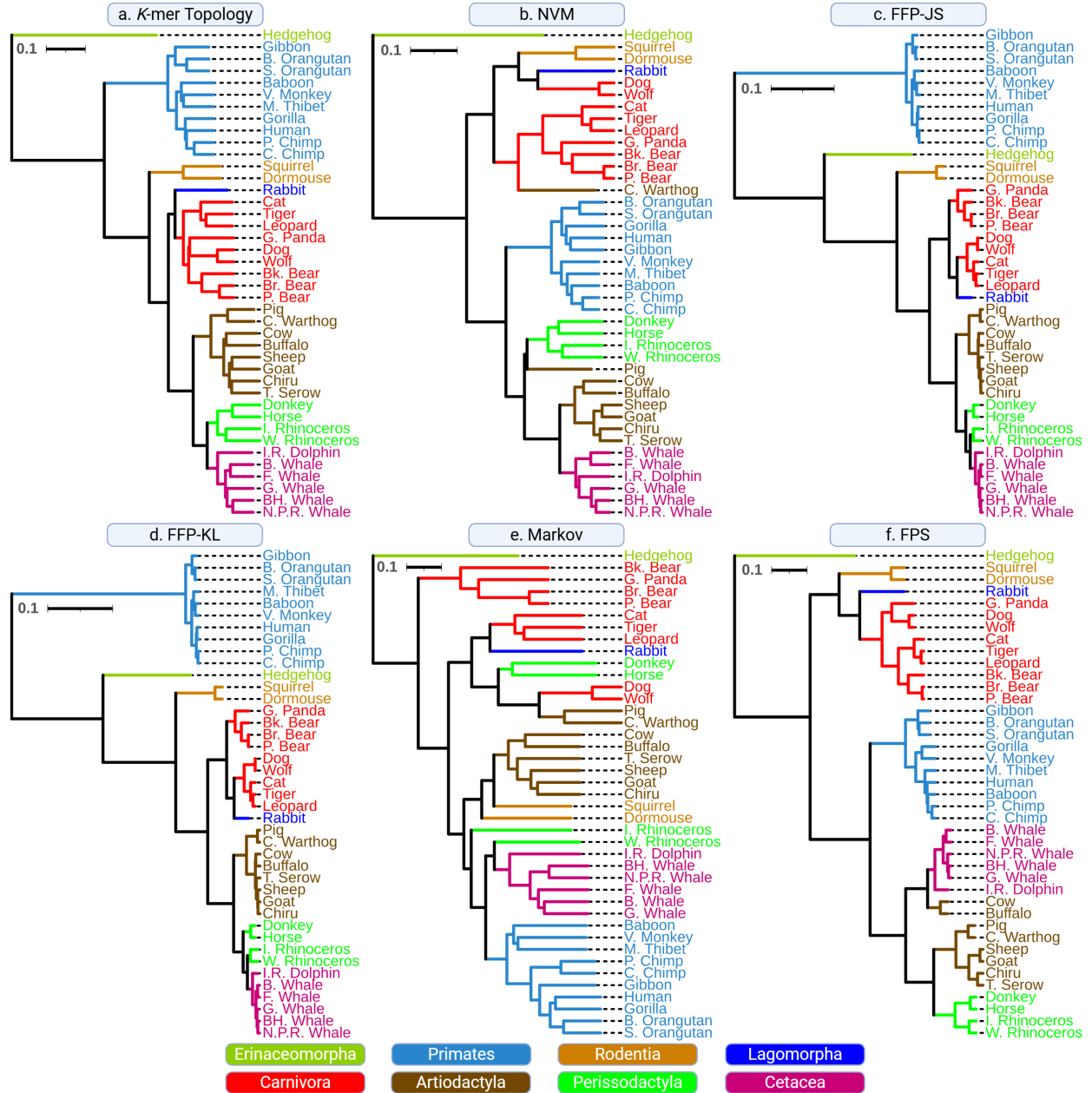


Figure 3: Phylogenetic tree analysis of 42 complete mammalian mitochondrial genomes. The mitochondrial genomes are categorized according to their host species classifications, including Artiodactyla, Carnivora, Cetacea, Erinaceomorpha, Lagomorpha, Perissodactyla, Primates, and Rodentia. The branches and labels are colored based on the host species classification. (a) K -mer topology with $K = 5$: All mitochondrial genomes are correctly classified into clades. (b) NVM using $k = 5$: The warthog and pig mitochondrial genomes are not clustered with the rest of the Artiodactyla mitochondrial genomes, and two separate clades of Carnivora mitochondrial genomes exist. (c) FFP-JS using $k = 3$: Two separate clades of Carnivora exist. Additionally, both rhinoceros mitochondrial genomes form a clade that is separated from the donkey and horse mitochondrial genomes. (d) FFP-KL using $k = 3$: Similar to FFP-JS, two clades of Carnivora and Perissodactyla mitochondrial genomes exist. (e) Markov K-String using $k = 3$: Three clades of Carnivora and two clades of Artiodactyla exist. Both Rodentia and Perissodactyla mitochondrial genomes do not form clades. (f) Fourier power spectrum method: Artiodactyla mitochondrial genomes form two clades.

2.3.2 Rhinovirus

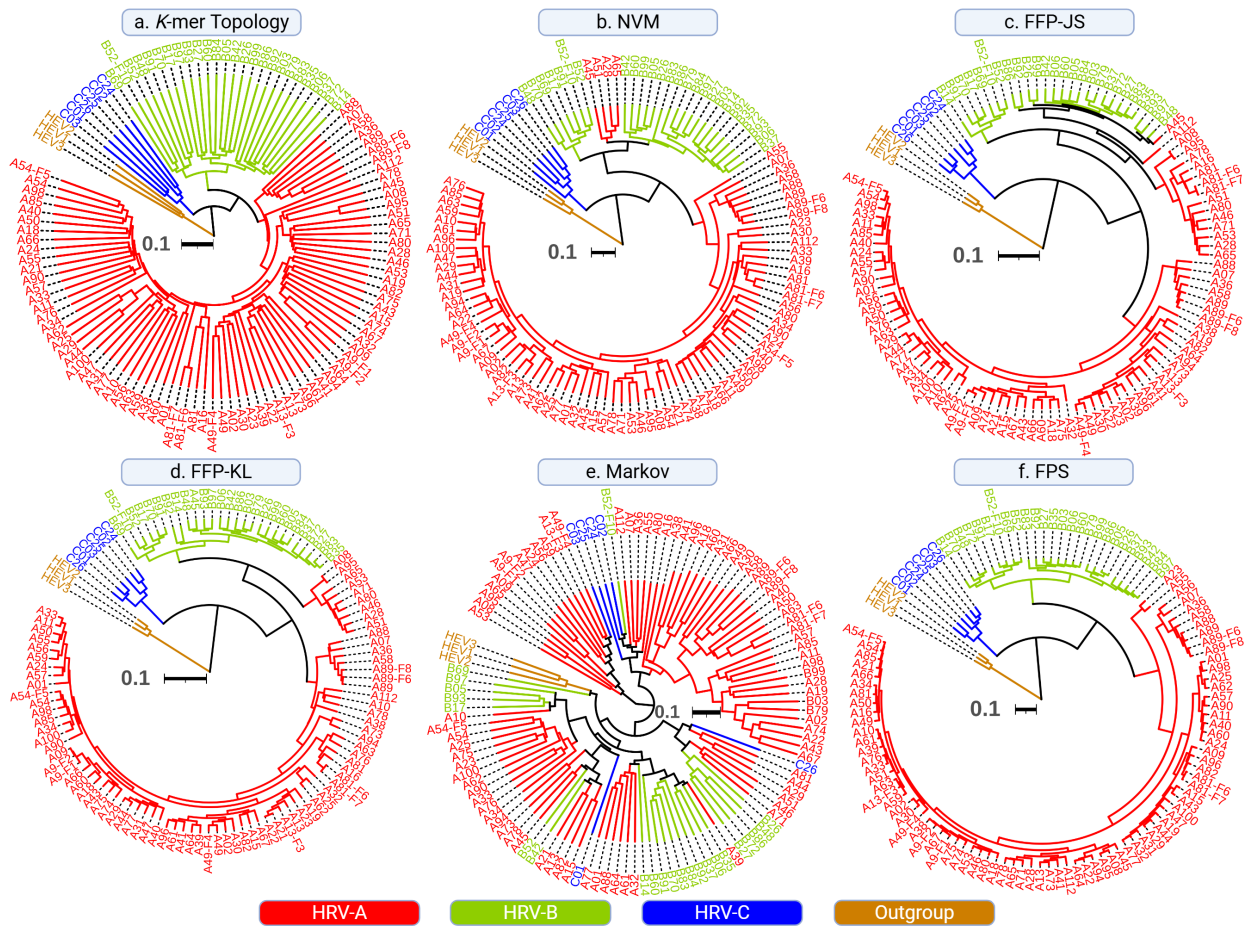


Figure 4: Phylogenetic tree analysis of 113 complete rhinovirus (HRV) genomes and 3 outgroup genomes. The HRV genomes are categorized into groups A, B, and C. The branches and labels are colored based on the HRV group, and the outgroup genomes are colored yellow. (a) K -mer topology using $K = 5$: All HRV genomes are correctly classified into clades, and the outgroup sequences form a separate clade from the HRV genomes. (b) NVM using $k = 5$: HRV genomes form a separate clade from the outgroup genomes. One HRV-A genome is placed within the HRV-B clade. (c) FFP-JS using $k = 3$: HRV genomes form a separate clade from the outgroup genomes. One HRV-A genome is placed within the HRV-B clade, and another HRV-A genome is within the HRV-B clade. (d) FFP-KL using $k = 3$: HRV genomes form a separate clade from the outgroup genomes. One HRV-A genome is placed within the HRV-B clade. (e) Markov K-String using $k = 3$: The outgroup genomes form a clade, but they do not form a separate clade from the HRV sequences. Although some groups form clusters, no uniform clade exists for each HRV group. (f) Fourier power spectrum method: All HRV genomes are correctly classified into clades, and the outgroup sequences form a separate clade from the HRV genomes.

Figure 4 shows the comparison of six methods for the phylogenetic tree analysis of 113 complete genomes of rhinovirus (HRV) and 3 outgroup genomes. The HRV genomes are classified into 3 groups: A, B, and C. The k -mer topology and FPS successfully cluster all genomes into their respective clades. NVM, FPS-JS, and FPS-KL show similar results, where a small HRV-A clade is formed within the HRV-B clade. Markov does not form a meaningful clade for any of the HRV groups.

2.3.3 SARS-CoV-2 variants

Figure 5 shows the comparison of six methods for the phylogenetic tree analysis of 44 complete Severe Acute Respiratory Syndrome Coronavirus 2 (SARS-CoV-2) genomes. The sequences were obtained from GISAID and are labeled according to their variants, including Alpha, Beta, Gamma, Delta, Lambda, Mu, GH/490R, and Omicron. The branches and labels are colored according to their variants.

Analyzing variants within a species is often difficult for alignment-free methods due to the key difference between the variants being mutations in just a few nucleotides. However, these key mutations have been shown to increase the infectivity of SARS-CoV-2 [8]. Interestingly, all methods, except for our k -mer topology, fail to fully separate the variants into their respective clades. FFP-KL and FFP-JS have 4 misclassified sequences and 2 clades of Omicron variants. Markov has 5 misclassified sequences. NVM and FPS fail to show meaningful clustering of most variants. In fact, persistent homology-based k -mer topology has 4 misclassified sequences as shown in Figure S9. This motivates the use of persistent Laplacian to enhance the clustering result, and more details can be found in subsection 3.3.

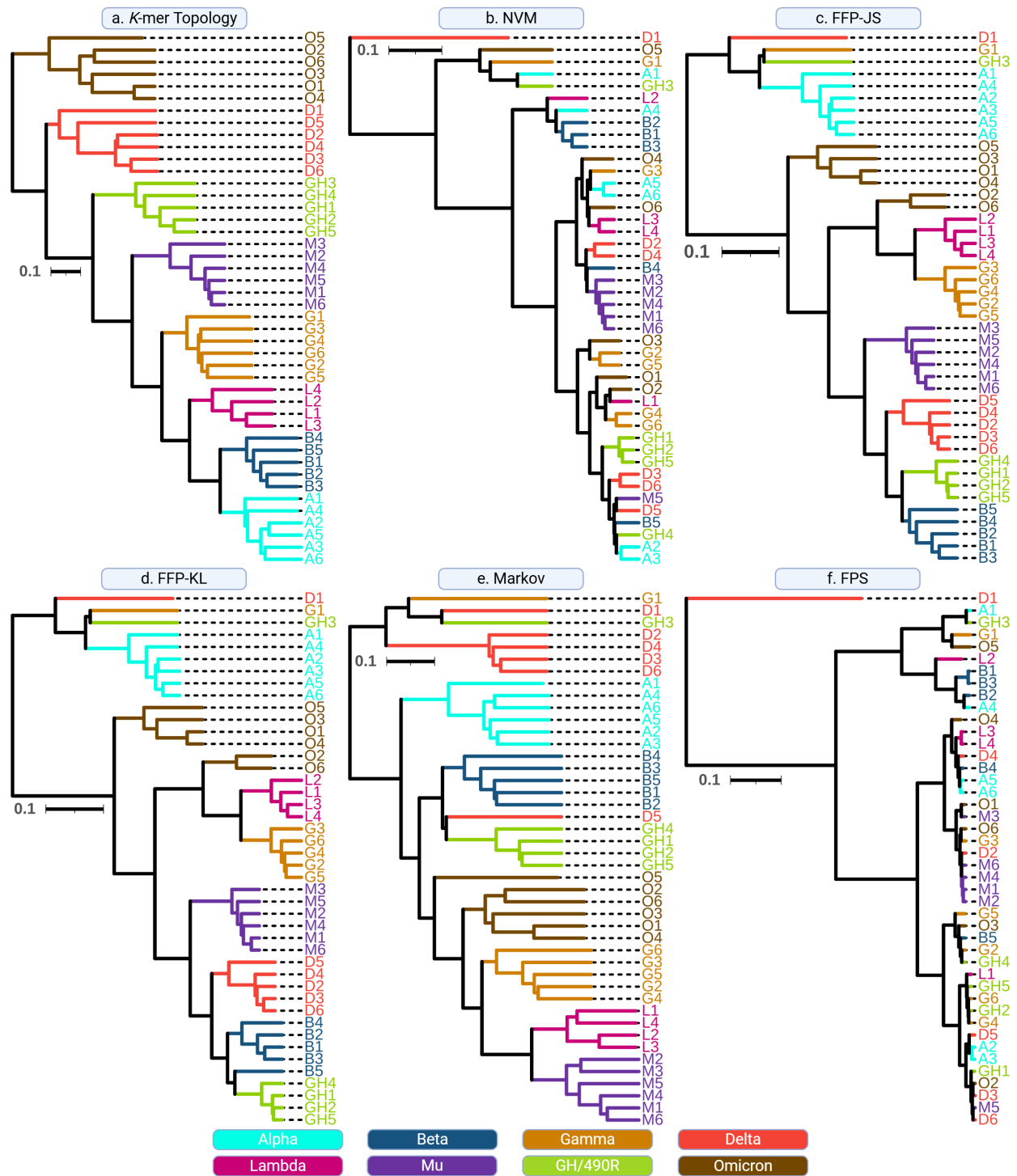


Figure 5: Phylogenetic tree analysis of 44 complete severe acute respiratory syndrome coronavirus 2 (SARS-CoV-2) genomes. The viral genomes are categorized according to their variants, including Alpha, Beta, Gamma, Delta, Lambda, Mu, GH/490R, and Omicron. Branches and labels are colored based on variant types. (a) *K*-mer topology using $k = 4$: All sequences are correctly clustered. (b) NVM using $k = 5$: Only the Mu and GH/490R variants show signs of clustering. (c) FFP-JS using $k = 3$: Three sequences—D1, G1, and GH3—are misclassified. Omicron sequences form two clades. (d) FFP-KL using $k = 3$: Three sequences—D1, G1, and GH3—are misclassified. Omicron sequences form two clades. (e) Markov K-String using $k = 3$: Five sequences—G1, D1, GH3, D5, and O5—are misclassified. All other sequences are clustered within their respective clades. (f) Fourier power spectrum method: No meaningful clusters are formed.

2.3.4 Hepatitis E virus

Figure S4 shows the comparison of six methods for the analysis of phylogenetic trees of 48 complete genomes of the hepatitis E virus (HEV). HEV viruses are categorized into 4 groups, and the branches and labels are colored according to their groups. K -mer topology, FFP-JS, and FFP-KL successfully cluster all sequences into their respective clade. NVM has 2 separate clades of group 3. Markov has 1 misclassified group 3 sequence (G3-17). FPS is unable to distinguish groups 3 and 4 HEV sequences.

2.3.5 Influenza A hemagglutinin genes

Figure S5 compares six methods for the phylogenetic tree analysis of 30 Influenza A hemagglutinin (HA) genes. The genes are categorized into six groups: H1N1, H2N2, H3N2, H5N1, H7N9, and H7N3. The branches and labels are color-coded according to the influenza A classifications.

K -mer topology, FFP-JS, and FFP-KL successfully cluster the genes into their respective clades. A notable difference is that, in FFP-JS and FFP-KL analyses, H3N3 and H2N2 share a node, while, in k -mer topology analysis, H3N3 and H2N2 are placed in different clades. NVM fails to group all H1N1 HA genes into a single clade and misclassifies one H2N2 sequence. Similarly, the Markov method misclassifies one H1N1 sequence. Lastly, FPS does not demonstrate clear clustering for most groups.

2.3.6 Ebola virus

Figure S6 compares six methods for the phylogenetic tree analysis of 59 ebola virus genomes. Ebola viruses are categorized into five types: Bundibugyo virus (BDBV), Reston virus (RESTV), Ebola virus (EBOV), Sudan virus (SUDV), and Tai Forest virus (TAFV). In addition, EBOV is further categorized according to the epidemic location and year. The branches are color-coded according to types of ebola viruses, and the labels are highlighted to represent specific epidemics.

All six methods successfully separate the types of ebola viruses into their respective clades. Furthermore, k -mer topology, NVM, FFP-JS, FFP-KL, and Markov separate the EBOV epidemics into individual clades. However, FFP-JS and FFP-KL show minimal differences between the various EBOV epidemics, as indicated by the short branch lengths. In contrast, k -mer topology and NVM display much longer branch lengths between EBOV epidemics, suggesting that these two methods better capture the finer differences among the epidemics. Markov produces a slightly different tree structure, where EBOV and RESTV share a node. FPS, while capable of separating the different types of ebola viruses, does not fully distinguish between EBOV epidemics.

2.3.7 Bacteria

To test the computational limits of k -mer topology, we performed a phylogenetic analysis on whole bacterial genomes. Figure S7 shows the comparison of the phylogenetic tree of 30 bacterial genomes. The genomes are categorized into nine families: *Bacillaceae*, *Borreliaceae*, *Burkholderiaceae*, *Clostridiaceae*, *Desulfovibrionaceae*, *Enterobacteriaceae*, *Rhodobacteraceae*, *Staphylococcaceae*, and *Yersiniaceae*.

Due to sequence lengths exceeding 1 million nucleotides, we utilized $k = 3, 4$, and 5 for k -mer topology. All six methods successfully separated the bacteria into their appropriate clades.

3 Discussion

We propose k -mer topology as a novel phylogenetic analysis method that utilizes persistent homology and/or persistent Laplacian for k -mer topological studies. Our method significantly outperforms other methods in viral classification tasks on different versions of viral data, indicating the robustness to changes in taxonomy.

We have also validated our method on standard phylogenetic analysis, including the whole bacteria sequence, indicating the robustness, reliability, and scalability of our method.

3.1 The shape of genome space from k -mer topology

It is interesting to understand why the proposed k -mer topology works so well for genome sequence analysis and prediction. In this approach, multiscale topological tools that can delineate the shape of the data [39] are used to characterize the shape of genome space. Topology is one of the most abstract subjects in mathematics that offers insights that cannot be obtained from any other mathematical, physical, and statistical approaches. Additionally, its abstraction dramatically simplifies data complexity. Moreover, persistent topology captures the multiscale relationship or intermittence patterns of k -mers in a genome sequence. Finally, the whole sequence topology does not contain enough information to depict the multifacet shape of a genome. The success of the k -mer topology is crucially attributed to the k -mer specific persistent topology.

3.2 Genome-specific k -mer distributions

We analyzed the k -mer distributions of 8 virus families: Adenoviridae, Circoviridae, Geminiviridae, Sedoreoviridae, Autographiviridae, Fiersviridae, Phenuiviridae, and Spinaeroviridae. To compare the distributions, we counted the average number of k -mers within a given radius of a nucleotide. Specifically, for each k -mer at l_p , we identified k -mer segments that were also within the radius r of l_p , and tracked the changes in the number of neighbors as the radius increased. We then normalized the counts to obtain the average number of k -mers in a given radius. Figure S8 visualizes the 16 2-mers of these viruses. Each plot corresponds to one of the 16 possible 2-mers, with color indicating the virus family. The x -axis represents the radius, while the y -axis shows the average 2-mer count. In particular, the distributions differ significantly between families. For example, Autographiviridae has the largest average AC count across all radii, but the lowest average TT count. These genome-specific distributions are characterized by the proposed k -mer topology.

3.3 Persistent Laplacian enhancement

While persistent homology provides detailed distributions of k -mers through persistent Betti numbers, it does not capture the complex geometric and topological information related to the evolution of homotopic shapes induced by filtration. To address this limitation, we incorporate persistent Laplacian [42] to obtain topological Laplacian spectra at each stage of filtration. The harmonic spectra (zero eigenvalues) return the persistent Betti numbers from persistent homology, while the non-harmonic spectra (non-zero eigenvalues) capture the evolution of the homotopic shapes of the genome data. This additional information is utilized to improve our k -mer topology analysis of genome sequences. A concise explanation of persistent Laplacian can be found in section 4. Figure S9 compares the characters derived from persistent homology (a) and persistent Laplacian (b) in the entire SARS-CoV-2 genome. SARS-CoV-2 variants were collected from GISAID (<https://gisaid.org/>), including Alpha, Beta, Gamma, Lambda, Mu, GH/490R, and Omicron variants. The clades and labels are color-coded according to the variants, with accession IDs for each label available in the supporting materials. In panel (a), Betti numbers for $k = 1, 2, 3$, and 4 were calculated, and the genetic distance was calculated using Equation 31 with $b_k = 0$ and $a_k = \frac{1}{\omega_k 2^{4-k}}$, where ω_k is the average k -mer distance between species. In panel (b), we include the spectra (the smallest nonzero eigenvalue) for each filtration value and used a multiscale distance on the Betti features to obtain a more detailed genetic distance. Details of the distance calculation can be found in Section S1 of the supporting materials. It is clear that the multiscale distance and the spectra feature significantly improve the clustering performance, enabling the k -mer topology to handle sequences with high similarities. However, it is important to note that calculating the Laplacian spectra is computationally expensive for larger sequences.

3.4 High-dimensional topological features

The inclusion of high-dimensional topological features has been examined, as detailed in the Methods section (see Figure 6(c)). High-dimensional topological features can certainly enhance the accuracy of the proposed k -mer topology. However, most genomes do not naturally possess high-order simplices. In fact, we can artificially create high-order simplices by connecting both ends of a sequence, as demonstrated in the Methods section. This approach generates non-trivial higher-order topological invariants that can further improve the accuracy of k -mer topology. However, the computation of higher-order simplicial complexes is typically time-consuming, and a balance must be struck between accuracy and computational efficiency.

3.5 Topological antigenetic distance

Antigenetic distance serves as a basis for the rational design of viral vaccines [47]. The superior performance of the k -mer topology in the phylogenetic tree analysis of various viruses suggests that the proposed topological genetic distance can be directly used as a reliable antigenetic distance. Our topological antigenetic distance can be applied to the rational design of viral vaccines to improve vaccine effectiveness against emerging viral variants.

3.6 Generalizations and applications

The proposed k -mer topology utilized only persistent homology and persistent Laplacian. It is important to explore further improvements of genome sequence analysis with other topological objects, such as path complexes, sheaf complexes, digraphs, hypergraphs, etc., and other topological formulations, such as quantum topology via Dirac, interaction topology, and Mayer topology. These improvements will be studied in future work.

Only the first non-harmonic eigenvalue of the persistent Laplacian was used in the present work. The inclusion of more non-harmonic eigenvalues may improve the present approach. This improvement is needed for the analysis of sequences with high similarity, such as SARS-CoV-2 variants.

Additionally, the computation of the proposed k -mer topology can be accelerated with parallel and GPU architectures because the calculations of each specific k -mer topology in a given sequence can be carried out independently of other k -mers and other sequences. Moreover, the computation of topological invariants can be improved. Fast algorithms for solving Laplacians can be implemented because only the first few eigenvalues are used. These accelerations are crucial for the whole-genome analysis of advanced biological species.

The proposed k -mer topology has potential applications in protein sequence alignment-free analysis, coding region identification, enhancer classification, etc.

4 Methods

In this section, we provide an overview of persistent homology of persistent topological Laplacian. Then, we provide the construction of the k -mer topology.

4.1 Persistent homology

Persistent homology is a new tool to analyze the shape of data [39, 48]. It utilizes concepts from algebraic topology, such as independent components, holes, and voids, to extract topological invariants from the data by representing point cloud data as simplicial complex, constructed from vertices, edges, triangles, and/or higher-order simplexes [49]. Filtration is applied to capture the persistence of these topological invariants across scales. Persistent homology was used in topological deep learning (TDL), coined in 2017 [50],

in predictions of protein-ligand binding affinities and changes in protein stability upon mutation. TDL outperforms other methods in the D3R Grand Challenges, a worldwide competition series in computer-aided drug design [51, 52].

4.1.1 Simplicial complex

We begin by providing a brief background on the simplicial complex. Let $\sigma_q = [v_0, \dots, v_q]$ be a q -simplex, where v_i is a vertex, and σ_q consists of $q+1$ vertices. For example, σ_0 is a node, σ_1 is an edge, σ_2 is a triangle, σ_3 is a tetrahedron, and so on. A simplicial complex K is a union of simplicies such that the following 2 properties hold.

1. If $\sigma_q \in K$, and σ_p is a face of σ_q , then $\sigma_p \in K$
2. The nonempty intersection of any 2 simplicies in K is a face of both simplicies.

In essence, one can view K as gluing together low-order simplicies.

4.1.2 Chain complex and homology groups

A q -chain is a formal sum of q -simplicies in K with coefficients \mathbb{Z}_2 . The set of all q -chains contain the basis for the set of q -simplicies in K , and this set form a finitely generated Abelian group $C_q(K)$ called the chain group. These chain groups are related by a boundary operator ∂_q , which is a group homomorphism $\partial_q : C_q(K) \rightarrow C_{q-1}(K)$. This boundary operator is defined as the following

$$\partial_q \sigma_q = \sum_{i=0}^q (-1)^i \sigma_{q-1}^i \quad (1)$$

where $\sigma_{q-1}^i = [v_0, \dots, v_i^*, \dots, v_q]$ is a $(q-1)$ -simplex with the vertex v_i removed from σ_q . Then, one can define the chain complex as a sequence of chain groups connected by these boundary operators.

$$\dots \xrightarrow{\partial_{q+2}} C_{q+1}(K) \xrightarrow{\partial_{q+1}} C_q(K) \xrightarrow{\partial_q} \dots \quad (2)$$

An important property of the boundary operator is that applying the boundary operator twice to any q -chain results in a mapping to a zero element. That is, $\partial_{q-1} \partial_q = \emptyset$. Additionally, the boundary operator for the 0-chain maps to 0, i.e., $\partial_0 = \emptyset$.

Using the boundary operators, one can define the q th cycle group Z_q and the q th boundary group B_q . Both Z_q and B_q are subgroups of the q th chain group C_q , and are defined as

$$Z_q = \text{Ker} \partial_q = \{c \in C_q \mid \partial_q c = \emptyset\} \quad (3)$$

$$B_q = \text{Im} \partial_{q+1} = \{c \in C_q \mid \exists d \in C_{q+1} : c = \partial_{q+1} d\} \quad (4)$$

Additionally, $\partial_{q-1} \partial_q = \emptyset$ implies that $B_q \subseteq Z_q \subseteq C_q$. Moreover, the q th cycle is the q -dimensional hole.

Using the groups one has defined, one can now define the homology group. The q th homology group, denoted H_q , is the quotient group generated by Z_q and B_q , i.e., $H_q = Z_q / B_q$. The rank of H_q is β_q , or the q th Betti number. When H_q is torsion free, the Betti number can be defined as

$$\beta_q = \text{rank} H_q = \text{rank} Z_q - \text{rank} B_q \quad (5)$$

The q th Betti number describes the q th dimensional hole. For example, β_0 is the number of connected components, β_1 is the number of loops, β_2 is the number of cavities, etc. Furthermore, the Betti numbers describe the topological property of the system.

4.1.3 Filtration and persistence

One downside of utilizing the simplicial complex is that it does not provide sufficient information to describe the geometry of the data because one can only capture the data in a single scale. To this end, one uses simplicial complex induced by filtration,

$$\emptyset = K_0 \subseteq \dots \subseteq K_p \subseteq \dots \subseteq K_P = K \quad (6)$$

where P is the number of filtration. Using such filtration is the foundation of persistent homology, where persistence is observed through long-lasting topological features. For each filtration p , one constructs the simplicial complex, the chain group, the subgroup, and the homology group. In particular, the p -persistent q -th homology group K^i is

$$H_q^{i,p} = Z_q^i / \left(B_q^{i+p} \cap Z_q^i \right) \quad (7)$$

Computing the Betti numbers gives the persistence of q -dimensional holes.

4.2 Persistent topological Laplacian

Although persistent homology can capture the persistence of topological invariants, it does not capture the homotopic shape evolution of the data. To this end, persistent spectral graph, also called persistent combinatorial Laplacian or persistent Laplacian, was proposed to obtain the spectra of topological Laplacians induced by filtration [42]. These spectra not only return all the topological invariant, namely persistent Betti numbers, from persistent homology, but also capture the homotopic shape evolution across scales. Persistent Laplacians have stimulated rapid theoretical developments [53–58] and successful applications [59–62], including forecasting of the emerging dominant SARS-CoV-2 variant BA.4 and BA.5 about two months in advance [8].

4.2.1 Topological Laplacian and its spectrum

The topological Laplacian provides insight into the structure of the simplicial complex. One can view topological Laplacian as an extension to the traditional graph Laplacian by analyzing higher-order topological structures. Note that standard graph Laplacian analysis can be viewed as analyzing the 1-simplices. For example, the multiplicity of 0-eigenvalue is the number of connected components, the first nonzero eigenvalue is the spectral gap, which is related to the Cheeger constant, and the second smallest non-zero eigenvalue relates to the algebraic connectivity. Furthermore, the collection of the eigenvalues of the graph Laplacian is called the Laplacian spectrum.

Traditionally, the graph Laplacian is computed by observing the adjacency matrix A and the degree matrix D of the graph, and computing $\mathcal{L} = D - A$. If we instead consider the graph as 1-simplex, we can compute the Laplacian matrix as $\mathcal{L} = B_1 B_1^T$, where B_1 is the 1-dimensional boundary operator matrix. Using this idea, we can extend this concept to higher-order simplices.

In order to define the topological Laplacian, we first define the dual chain complex through the adjoint operator of ∂_q which is defined in the dual spaces $C^q(K) \equiv C_q^*(K)$. The coboundary operator $\partial_q^* : C^{q-1}(K) \rightarrow C^q(K)$ is defined as

$$\partial_q^* \omega^{q-1}(c_q) \equiv \omega^{q-1}(\partial c_q) \quad (8)$$

where $\omega^{q-1} \in C^{q-1}(K)$ and $c_q \in C_q(K)$. Here, ω^{q-1} is the $(q-1)$ cochain, which is a homomorphism mapping of a chain to the coefficient group. The homology of the dual chain complex is called cohomology.

We can now define the q -combinatorial Laplacian operator $\Delta_q : C^q(K) \rightarrow C^q(K)$ as

$$\Delta_q := \partial_{q+1} \partial q + 1^* + \partial_q^* \partial q. \quad (9)$$

Denoting \mathcal{B}_q as the standard basis of the q -boundary operator from $C_q(K)$ and $C_{q-1}(K)$ and \mathcal{B}_q^T as the basis for the q -boundary operator, we can obtain the matrix representation of the q -th order Laplacian operator \mathcal{L}_q , which is defined as

$$\mathcal{L}_q = \mathcal{B}_{q+1} \mathcal{B}_{q+1}^T + \mathcal{B}_q^T \mathcal{B}_q. \quad (10)$$

The multiplicity of the zero eigenvalues of \mathcal{L}_q is the q th Betti number, and the nonzero eigenvalues, or the non-harmonic spectra, contain other topological and geometrical features.

4.2.2 Filtration and persistence

Similarly to persistent homology, we can introduce filtration to obtain the persistence of topological invariants and the evolution of homotopic shapes. For each K_p $0 \leq p \leq P$, denote $C_q(K_p)$ as the chain group induced by K_p , and the corresponding boundary operator $\partial_q^p : C_q(K_p) \rightarrow C_{q-1}(K_p)$ defined as

$$\partial_q^p \sigma_q = \sum_{i=0}^q (-1)^i \sigma_{q-1}^i \quad (11)$$

for $\sigma_q \in K_p$. Similarly, the adjoint operator is defined as $\partial_q^{p*} : C^{q-1}(K_p) \rightarrow C^q(K_p)$.

Now, we can define the spectra of the persistent Laplacian. Denote $\mathbb{C}_q^{p,t}$ as the $C_q^{p,t}$ whose boundary is in C_{q-1}^p , assuming an inclusion mapping $C_{q-1}^p \rightarrow C_{q-1}^{p,t}$. In such a set, we can define the t -persistent q -boundary operator $\hat{\partial}_q^{p,t} : \mathbb{C}_q]p, t \rightarrow C_{q-1}^p$, and its corresponding adjoint operator $(\hat{\partial}_q^{p,t})^* : C_{q-1}^p \rightarrow \mathbb{C}_q^{p,t}$. Then, the q -order t -persistent Laplacian operator can be obtained via

$$\Delta_q^{p,t} = \hat{\partial}_{q+1}^{p,t} (\hat{\partial}_{q+1}^{p,t})^* + (\hat{\partial}_q^{p,t})^* \hat{\partial}_q^{p,t}. \quad (12)$$

Similarly, using the standard basis for the matrix representation of the operators, we obtain the q -order t -persistent Laplacian operator $\mathcal{L}_q^{p,t}$

$$\mathcal{L}_q^{p,t} = \mathcal{B}_{q+1}^{p,t} (\mathcal{B}_{q+1}^{p,t})^T + (\mathcal{B}_q^p)^T (\mathcal{B}_q^p). \quad (13)$$

4.3 K -mer topology for nucleotide sequences

In this section, we describe the persistent topology for nucleotide sequences, and the extraction of topological and algebraic features. Then, we define a distance metric on the features for phylogenetic analysis. Figure 6 shows the feature extraction procedure using a randomly generated sequence.

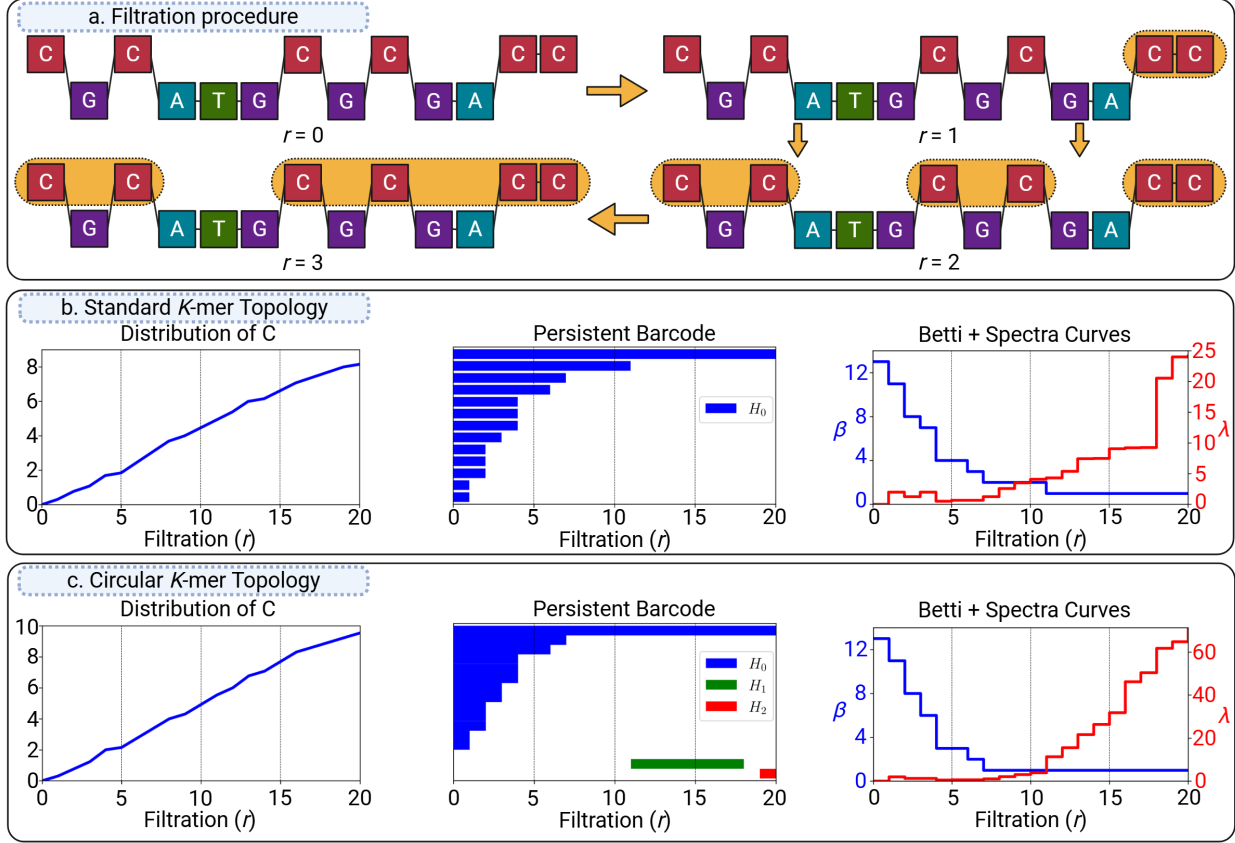


Figure 6: Feature extraction procedure using nucleotide C with a randomly generated sequence of length 50. (a) The filtration procedure using nucleotide C . C 's connected by the orange bar indicates a connected component. (b) The distribution of C , persistent barcode and the topological curves for the standard K -mer topology, where the sequence is considered a line. (c) The distribution of C , persistent barcode, and the topological curves for the circular K -mer topology, where the ends of the sequence is connected into a circle. For the distribution, the average number of nucleotide C was counted at different filtration radius. In the persistent barcode, the blue, green and red barcodes correspond to persistent Betti-0, Betti-1, and Betti-2, respectively. The blue and red line in the topological curves correspond to the Betti and smallest nonzero eigenvalue, respectively, at different filtration radius.

4.3.1 Position based distance

Let $S = s_1 s_2 \dots s_N$ be a DNA sequence of length N , where $s_i \in \{A, C, G, T\}$ is a nucleotide. Define the nucleotide-specific indicator function $\delta_l(s_i)$ as

$$\delta_l(s_i) = \begin{cases} 1, & s_i = l \\ 0, & \text{otherwise,} \end{cases} \quad (14)$$

where $l \in \{A, C, G, T\}$. Then, we can define a set of nucleotide specific positions S^l as

$$S^l = \{i | \delta_l(s_i) = 1, 1 \leq i \leq N\}. \quad (15)$$

The set S^l contains all the global positions of nucleotide type l . Then, we can compute the pairwise distance matrix of the nucleotide type l

$$D^l = \{d_{ij}^l\}, \quad d_{ij}^l = |S^l(i) - S^l(j)|, \quad (16)$$

where $1 \leq i, j \leq |S^l|$, and $|S^l|$ is the total number of nucleotide type l .

In general, we can define a set of k -mer-specific positions, where instead of looking only at a specific nucleotide, we look at a given string of nucleotides of length k , i.e., a k -mer type. Moreover, there are 4^k different combinations of k -mers for a given k , which we denote as l_1, l_2, \dots, l_{4^k} . Similarly, we can define the k -mer specific indicator function as

$$\delta_{l_p}(s_i s_{i+1} \dots s_{i+k}) = \begin{cases} 1, & s_i s_{i+1} \dots s_{i+k} = l_p \\ 0, & \text{otherwise.} \end{cases} \quad (17)$$

Then, the set of k -mer specific positions S^{l_p} is given by

$$S^{l_p} = \{i | \delta_{l_p}(s_i s_{i+1} \dots s_{i+k}) = 1, 1 \leq i \leq N - k + 1\}. \quad (18)$$

Then the k -mer specific distance matrix for k -mer type l_p is given by

$$D^{l_p} = \{d_{ij}^{l_p}\}, \quad d_{ij}^{l_p} = |S^{l_p}(i) - S^{l_p}(j)|. \quad (19)$$

Distance matrices are used to compute both persistent homology and persistent Laplacians features.

4.3.2 Persistent Laplacian features

For feature generation, we begin by constructing a series of graph Laplacian induced by filtration. For $0 \leq p \leq P$, let $L_{0,r}^{l_p}$ be the l_p -specific 0-order r -th graph Laplacian, which can be computed as the following

$$L_{0,r}^{l_p} = \{(l_{0,r}^{l_p})_{ij}\}, \quad (l_{0,r}^{l_p})_{ij} = \begin{cases} -1, & d_{ij}^{l_p} \leq r, i \neq j \\ \sum_j (l_{0,r}^{l_p})_{ij}, & i = j. \end{cases} \quad (20)$$

We can order the eigenvalues of $L_{0,r}^{l_p}$ as $0 = \lambda_1 \leq \lambda_2 \leq \dots \leq \lambda_{|S^{l_p}|}$. The number of non-zero eigenvalues is the 0-Betti number, denoted $\beta_{0,r}^{l_p}$, and the smallest non-zero eigenvalue is denoted $\lambda_{r,0}^{l_p}$.

For each k -mer type l_p , we can collect persistent Betti numbers and the smallest non-zero eigenvalues to obtain the k -mer specific $\beta_0^{l_p}$ and $\lambda_0^{l_p}$.

$$\boldsymbol{\beta}_0^{l_p} = (\beta_{0,r_1}^{l_p}, \beta_{0,r_2}^{l_p}, \dots) \quad (21)$$

$$\boldsymbol{\lambda}_0^{l_p} = (\lambda_{0,r_1}^{l_p}, \lambda_{0,r_2}^{l_p}, \dots) \quad (22)$$

where r_1, r_2, \dots is the increasing filtration radius.

Now, consider a sequence of length 13 shown in Figure 6. The k -mer positions can be described in Table 1.

Table 1: Sample sequence CGCATGCGCGACC and the positron of the k -mers.

Position	1	2	3	4	5	6	7	8	9	10	11	12	13
Sequence	C	G	C	A	T	G	C	G	C	G	A	C	C
1-mer	C	G	C	A	T	G	C	G	C	G	A	C	C
2-mer	CG	GC	CA	AT	TG	GC	CG	GC	CG	GA	AC	CC	-
3-mer	CGC	GCA	CAT	ATG	TGC	GCG	CGC	GCG	CGA	GAC	ACC	-	-

We can compute S^C and D^C as

$$S^C = \{1, 3, 6, 8\}, \quad D^C = \begin{pmatrix} 0 & 2 & 5 & 7 \\ 2 & 0 & 3 & 5 \\ 5 & 3 & 0 & 2 \\ 7 & 5 & 2 & 0 \end{pmatrix}. \quad (23)$$

Using the same sequence in Table 1, then 2-mer CG specific positions and distances can be defined as the following

$$S^{\text{CG}} = \{1, 6, 8\}, \quad D^{\text{CG}} = \begin{pmatrix} 0 & 5 & 7 \\ 5 & 0 & 2 \\ 7 & 5 & 0 \end{pmatrix}. \quad (24)$$

Similarly, the 3-mer CGC specific positions and distances can be defined as the following

$$S^{\text{CGC}} = \{1, 6\}, \quad D^{\text{CGC}} = \begin{pmatrix} 0 & 5 \\ 5 & 0 \end{pmatrix}. \quad (25)$$

We illustrate an example of our method using the influenza haemagglutinin (HA) gene of H1N1. In Figure S10, we generated 2 cases of the K -mer topology by treating the DNA sequence as a line and as a circle, and utilized the k -mer AC. The upper row shows the standard case, and the bottom row shows the circular case. In the circular case, the distance between the k -mers is modified, by taking

$$d^l(i, j) = \min[S^l(j) - S^l(i), N - S^l(j) + S^l(i)]. \quad (26)$$

By doing so, the sequence is allowed to wrap around. The first column shows the average number of AC within the filtration radius r . Not surprisingly, the average number of AC is slightly higher for the circular case. The second column shows the Betti-0 number as we increase the filtration radius. Interestingly, the Betti-0 number remains similar for both cases; however, the circular case has lower values of Betti-0. This is because by allowing the sequence to wrap around, the ACs at the 5' and 3' ends are allowed to form connected components. Nonetheless, the difference is very small. The third column shows the smallest non-zero eigenvalue as we increase the filtration radius. Interestingly, the behavior is similar until $r = 40$. However, because we allow the sequence to wrap around, the number of edges in our Laplacian graph is significantly higher for the circular case. This most likely led to a larger eigenvalue as the filtration radius increased.

4.3.3 Topological genetic distance

We now define a topological metric for perform phylogenetic analysis. For each k , we have 4^k different k -mers specific Betti-0 and minimal eigenvalue curves. We concatenate these curves to obtain the vector

$$\beta^k = (\beta_0^{l_1}, \dots, \beta_0^{l_{4^k}}) \quad (27)$$

$$\lambda^k = (\lambda_0^{l_1}, \dots, \lambda_0^{l_{4^k}}). \quad (28)$$

Then, for sequences i and j , we can define the topological metric between the k -mer specific curves as the following

$$\text{dist}_\beta^k(i, j) = \|\beta_i^k - \beta_j^k\|_2 \quad (29)$$

$$\text{dist}_\lambda^k(i, j) = \|\lambda_i^k - \lambda_j^k\|_2, \quad (30)$$

where $\|\cdot\|_2$ denote the Euclidean distance.

Then, we can take a weighted sum over different k to obtain a topological genetic distance between sequences i and j

$$\text{Dist}(i, j) = \sum_{k=1}^K a_k \text{dist}_\beta^k(i, j) + b_k \text{dist}_\lambda^k(i, j). \quad (31)$$

If we only need Betti-0 features, we set $b_k = 0$, and in this work, we utilized $a_k = \frac{1}{\omega_k 2^{K-k}}$ and $b_k = 0$, where K is the largest k , and ω_k is the average dist_β^k . Alternative definitions of topological genetic/antigenetic distances are presented in the Supporting Information.

Data and code availability

Datasets are available from the NCBI virus database, <https://www.ncbi.nlm.nih.gov/labs/virus/vssi/>, which was accessed in March 2024. NCBI 2020 and 2022 can be accessed from [44] and [63], respectively. All codes, including those of other methods compared in this work, are available on Github, <https://github.com/hozumiyu/KmerTopology>, and are further described in the Supporting Information.

Supporting Information

Supporting Information is available.

Acknowledgment

This work was supported in part by NIH grants R01AI164266, and R35GM148196, NSF grants DMS-2052983 and IIS-1900473, MSU Research Foundation, and Bristol-Myers Squibb 65109.

S1 Topological genetic/antigenetic distances

Genetic distance and antigenetic distance have a wide variety of applications, including the rational design of vaccines against viruses, such as SARS-CoV-2 [47] and influenza [64]. Specifically, antigenetic distance can be used to predict vaccine effectiveness against viral variants. This approach becomes very powerful when combined with deep mutational scanning [65,66] and the accurate forecasting of emerging viral variants [7,8], offering rapid responses to fast viral evolution [67].

In the main text, we define a topological genetic distance for classification and clustering. That is, for sequences i and j , the genetic distance between them is given by

$$\text{Dist}(i, j) = \sum_{k=1}^K a_k \text{dist}_{\beta}^k(i, j) + b_k \text{dist}_{\lambda}^k(i, j) \quad (\text{S1})$$

for some hyperparameters a_k and b_k . If we only consider Betti-0 features, we can set $b_k = 0$ for all k . In our benchmark, we set $a_k = \frac{1}{\omega_k 2^{K-k}}$, where K is the maximum k -mer we consider, and ω_k is the average $\text{dist}_{\beta}^k(i, j)$. One potential downside to this approach is that the distance can be dominated by some large Betti numbers (that is, those in the first few filtration steps) and large spectra.

For a more detailed analysis, it may be more feasible to consider multiscale distance calculations, where the distance is calculated for each filtration radius. For each k , we have l_{4^k} combinations of k -mers. Denote $\beta_{k,r}$ as the Betti number for a given k and a given filtration radius.

$$\beta_{k,r} = (\beta_r^{l_1}, \beta_r^{l_2}, \dots, \beta_r^{l_{4^k}}) \quad (\text{S2})$$

Similarly, we can define $\lambda_{k,r}$ as the smallest nonzero eigenvalue for a given k and a given filtration radius.

$$\lambda_{k,r} = (\lambda_r^{l_1}, \lambda_r^{l_2}, \dots, \lambda_r^{l_{4^k}}) \quad (\text{S3})$$

Then, we can consider the distance between sequences i and j for k -mer l_{4^k} at radius r to be

$$\text{dist}_{\beta_{k,r}}(i, j) = \|\beta_{k,r}(i) - \beta_{k,r}(j)\| \quad (\text{S4})$$

$$\text{dist}_{\lambda_{k,r}}(i, j) = \|\lambda_{k,r}(i) - \lambda_{k,r}(j)\|. \quad (\text{S5})$$

Then, the genetic distance will be the weighted sum of these multiscale distances.

$$\text{Dist}(i, j) = \sum_r \sum_{k=1}^K a_{k,r} \text{dist}_{\beta_{k,r}}(i, j) + b_{k,r} \text{dist}_{\lambda_{k,r}}(i, j) \quad (\text{S6})$$

We validated this approach for SARS-CoV-2 classification in Figure S9. We let $K = 4$, $a_{k,r} = \frac{1}{\omega_{k,r} 2^{4-k}}$, $b_{k,r} = \frac{1}{\gamma_k 2^{4-k}}$, and $\omega_{k,r}$ is the average $\text{dist}_{\beta_{k,r}}$, and γ_k is the average $\text{dist}_{\lambda_{k,r}}$. For this analysis, we do not use multiscale distances for the spectra curves.

The classification of SARS-CoV-2 variants is extremely challenging for alignment-free methods because the defining mutations on the variants are only a few nucleotides. We can see in Figure 5 that none of the 5 other alignment-free methods can classify the variants properly. However, by introducing the multiscale distance, k -mer topology can successfully capture the small mutational differences.

S2 Additional classification benchmark

In Tables S1, S1, and S2, we present more details on the classification of four viral datasets. Six methods, including k -mer topology, NVM, FFP-JS, FFP-KL, Markov and FPS, were employed in the comparative analysis.

Table S1 shows the accuracy comparison of k -mer topology, NVM, FFP-JS, FFP-KL, Markov and FPS methods for the 1-nearest neighbor classification of 4 benchmark datasets. The bold values indicate the best accuracy for each data. Our method outperforms other methods by a large margin on all datasets.

Table S1: 1-NN classification accuracy of 6 methods.

Data	Method					
	k -mer topology	NVM	FPS-JS	FFP-KL	Markov	FPS
NCBI 2020	0.933	0.879	0.862	0.862	0.734	0.732
NCBI 2022	0.920	0.875	0.870	0.870	0.735	0.732
NCBI 2024	0.898	0.829	0.825	0.826	0.637	0.656
NCBI 2024 All	0.901	0.825	0.832	0.832	0.647	0.647

Figure S1 shows the benchmark comparison of our method with the 5 other methods on 4 datasets. For each dataset, stratified 5-fold cross validation with 30 random seeds was used to obtain the scores. Accuracy (ACC), balanced accuracy (BA), macri-F1 (F1), area under the receiving operator curve (AUC-ROC), recall, and precision were used to evaluate the classification performance. Macro scores were used for all tests because each viral family is equally important. Additionally, for AUC-ROC, one-versus-rest was used to obtain the scores. K -mer topology out performs all other methods in every metric across all datasets.

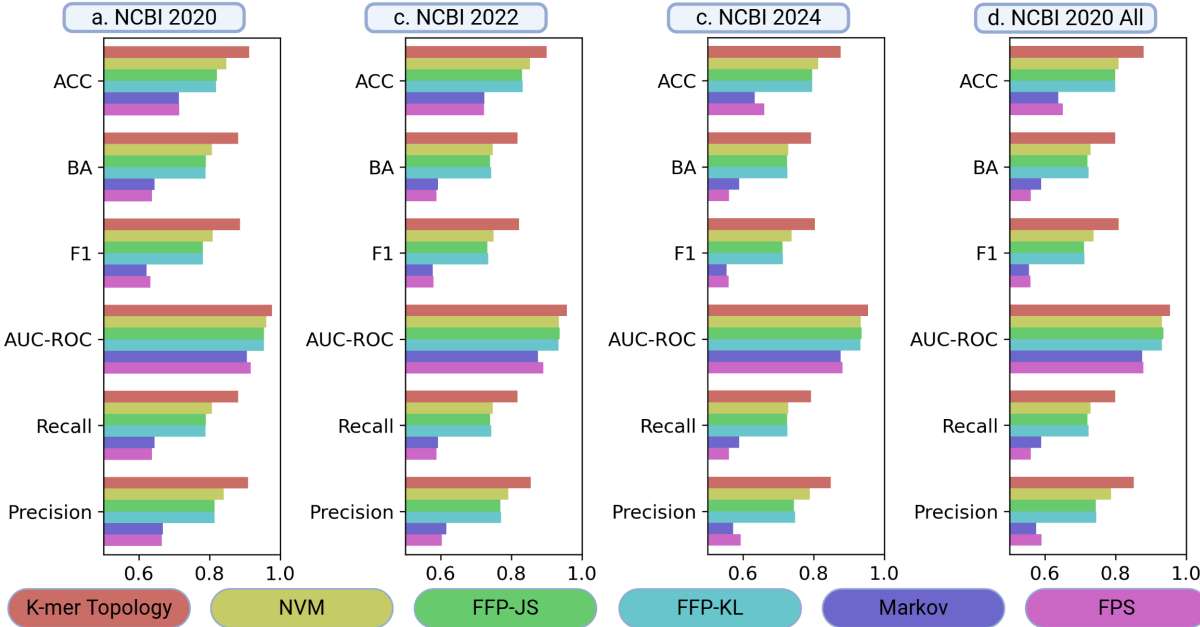


Figure S1: Comparison of six methods for 5-nearest neighbor classification of the NCBI virus datasets. Stratified 5-fold cross validation with 30 random seeds was performed. (a)NCBI 2020. (b) NCBI 2022. (c) NCBI 2024. (d) NCBI 2024 All. Accuracy (ACC), balanced accuracy (BA), macri-F1 (F1), area under the receiving operator curve (AUC-ROC), recall, and precision were used to evaluate the classification performance.

Table S2 shows the ACC, BA, F1, AUC-ROC, recall, and precision of 5-NN classification. The bold values indicate the best scores for each dataset and scores.

Table S2: Comparison of 5-NN classification scores of the 6 methods.

Data	Method	Scores					
		ACC	BA	F1	AUC-ROC	Recall	Precision
NCBI 2020	<i>k</i> -mer topology	0.912	0.881	0.886	0.977	0.881	0.909
	NVM	0.847	0.807	0.809	0.960	0.807	0.840
	FFP-JS	0.821	0.790	0.781	0.954	0.790	0.814
	FFP-KL	0.819	0.789	0.780	0.954	0.789	0.814
	Markov	0.713	0.644	0.622	0.905	0.644	0.668
	FPS	0.714	0.637	0.633	0.917	0.637	0.665
NCBI 2022	<i>k</i> -mer topology	0.900	0.818	0.821	0.957	0.818	0.855
	NVM	0.852	0.747	0.750	0.935	0.747	0.791
	FFP-JS	0.830	0.740	0.733	0.937	0.740	0.769
	FFP-KL	0.832	0.743	0.735	0.934	0.743	0.771
	Markov	0.724	0.593	0.577	0.876	0.593	0.617
	FPS	0.723	0.588	0.580	0.890	0.588	0.603
NCBI 2024	<i>k</i> -mer topology	0.877	0.793	0.803	0.954	0.793	0.848
	NVM	0.814	0.729	0.738	0.933	0.729	0.789
	FFP-JS	0.796	0.724	0.712	0.936	0.724	0.744
	FFP-KL	0.796	0.727	0.714	0.932	0.727	0.747
	Markov	0.633	0.589	0.554	0.876	0.589	0.573
	FPS	0.660	0.561	0.560	0.882	0.561	0.593
NCBI 2024 All	<i>k</i> -mer topology	0.880	0.799	0.808	0.954	0.799	0.851
	NVM	0.809	0.729	0.738	0.931	0.729	0.788
	FFP-JS	0.799	0.721	0.711	0.935	0.721	0.745
	FFP-KL	0.799	0.724	0.712	0.931	0.724	0.745
	Markov	0.638	0.589	0.555	0.876	0.589	0.575
	FPS	0.651	0.561	0.559	0.879	0.561	0.591

1.

S3 Additional materials for phylogenetic analysis using *k*-mer topology

In this section, we compare the phylogenetic trees generated from the *k*-mer topology with those from natural vector method (GNV) [44], Markov K-string [20], KL-and JS divergence of *k*-mers frequency profile, and Fourier power spectrum (FPS) method [35]. For Markov K-String, KL divergence and JS divergences, $k = 3$ was used to obtain the features. To build up phylogenetic trees, unweighted pair group method with arithmetic mean (UPGMA) was used, and interactive tree of life v6 [68] was used to generate and annotate the trees.

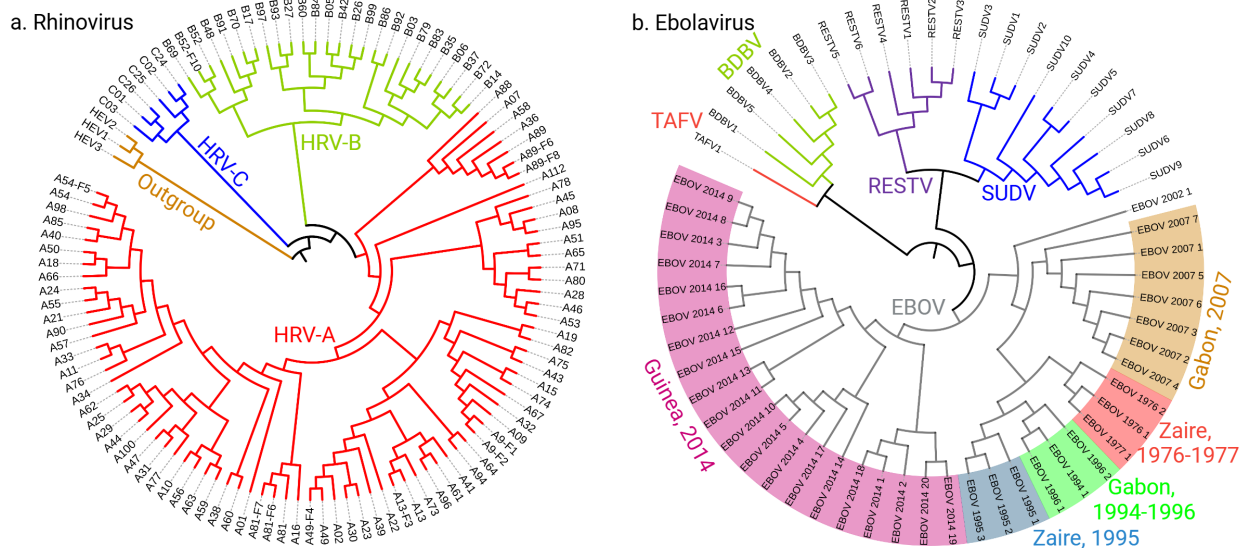


Figure S2: (a) Phylogenetic tree of rhinovirus (HRV) using $k = 5$. The data contains three HRV groups—A, B, and C—along with three outgroup sequences. The K -mer topology places the outgroup sequences in an entirely separate clade and distinguishes each HRV group into individual clades. (b) Phylogenetic tree of ebola virus using $k = 5$. The data contains five types: Tai Forest virus (TAFV), Sudan virus (SUDV), Bundibugyo virus (BDBV), Reston virus (RESTV), and ebola virus (EBOV). Additionally, EBOV is categorized by pandemic year and location, with labels highlighted according to their respective locations. The K -mer topology places each type into distinct clades and further separates the EBOV subtypes.

Figure S2 shows the phylogenetic tree of rhinovirus and ebola virus using our method with $k = 5$. Figure S3 shows the phylogenetic trees of influenza A haemagglutinin genes, mammalian mitochondria, bacteria and hepatitis E virus generated using our method. Our K -mer topology successfully clusters all genomes into their respective classifications. We provide a more thorough comparative analysis in the subsequent subsections.

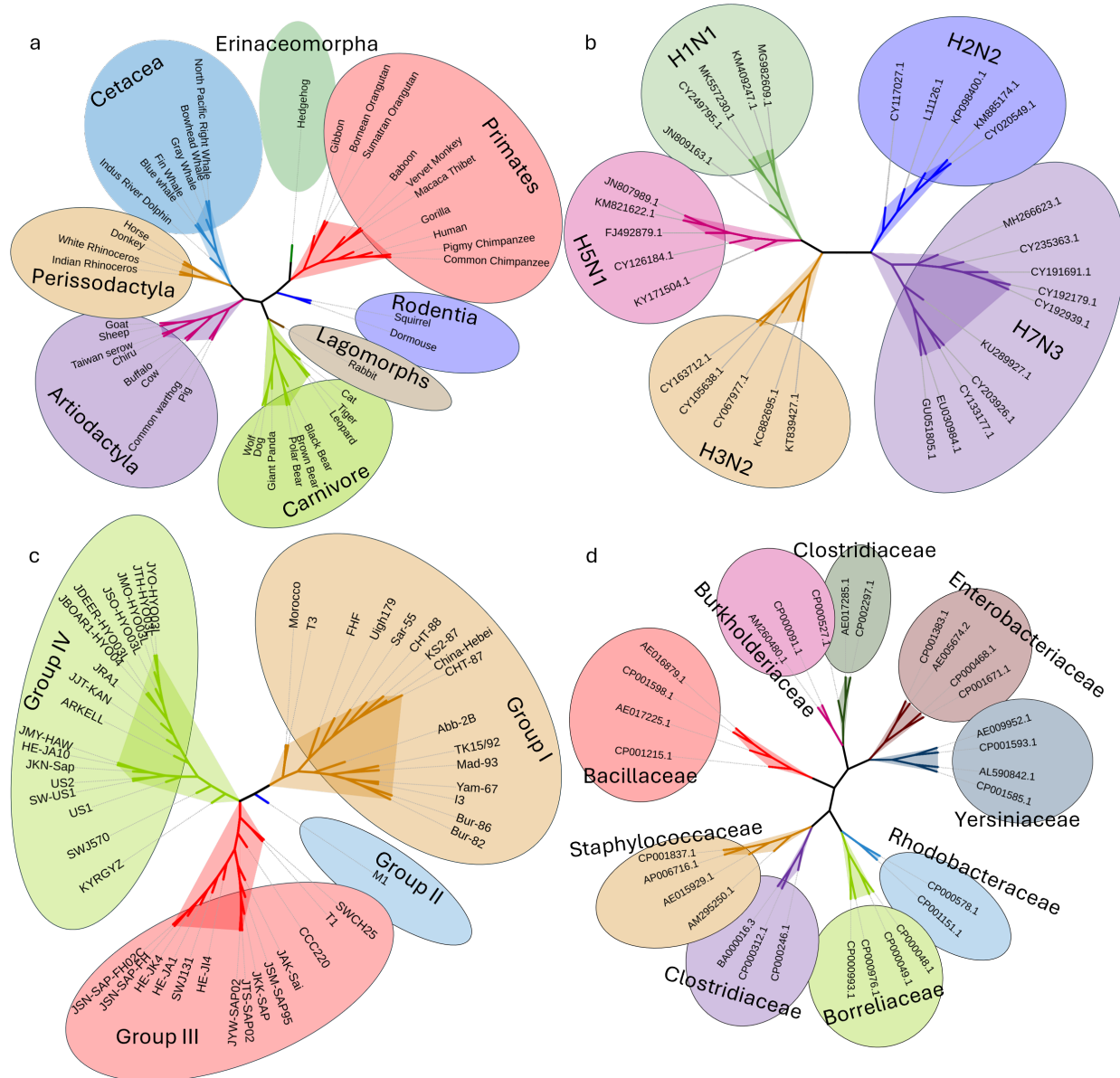


Figure S3: Phylogenetic analysis using K -mer topology. (a) Phylogenetic tree of the influenza A haemagglutinin genes using $k = 3$. The data contains six types: H1N1, H2N2, H7N9, H7N3, H3N3, and H5N1. The K -mer topology separates all six types into distinct clades. (b) Phylogenetic tree of complete mammalian mitochondrial genomes using $k = 5$. The data contains eight host species types, with mitochondrial genomes categorized according to their host species. The K -mer topology separates all eight types into distinct clades. (c) Phylogenetic tree of complete bacterial genomes using $k = 5$. Because the sequence length exceeds 1 million base pairs, 3-mers, 4-mers, and 5-mers were used. The data contains nine bacterial families, and the K -mer topology separates all nine families into distinct clades. (d) Phylogenetic tree of hepatitis E virus (HEV) using $k = 5$. The data contains four groups. The K -mer topology separates all four groups into distinct clades.

S3.1 Hepatitis E virus genomes

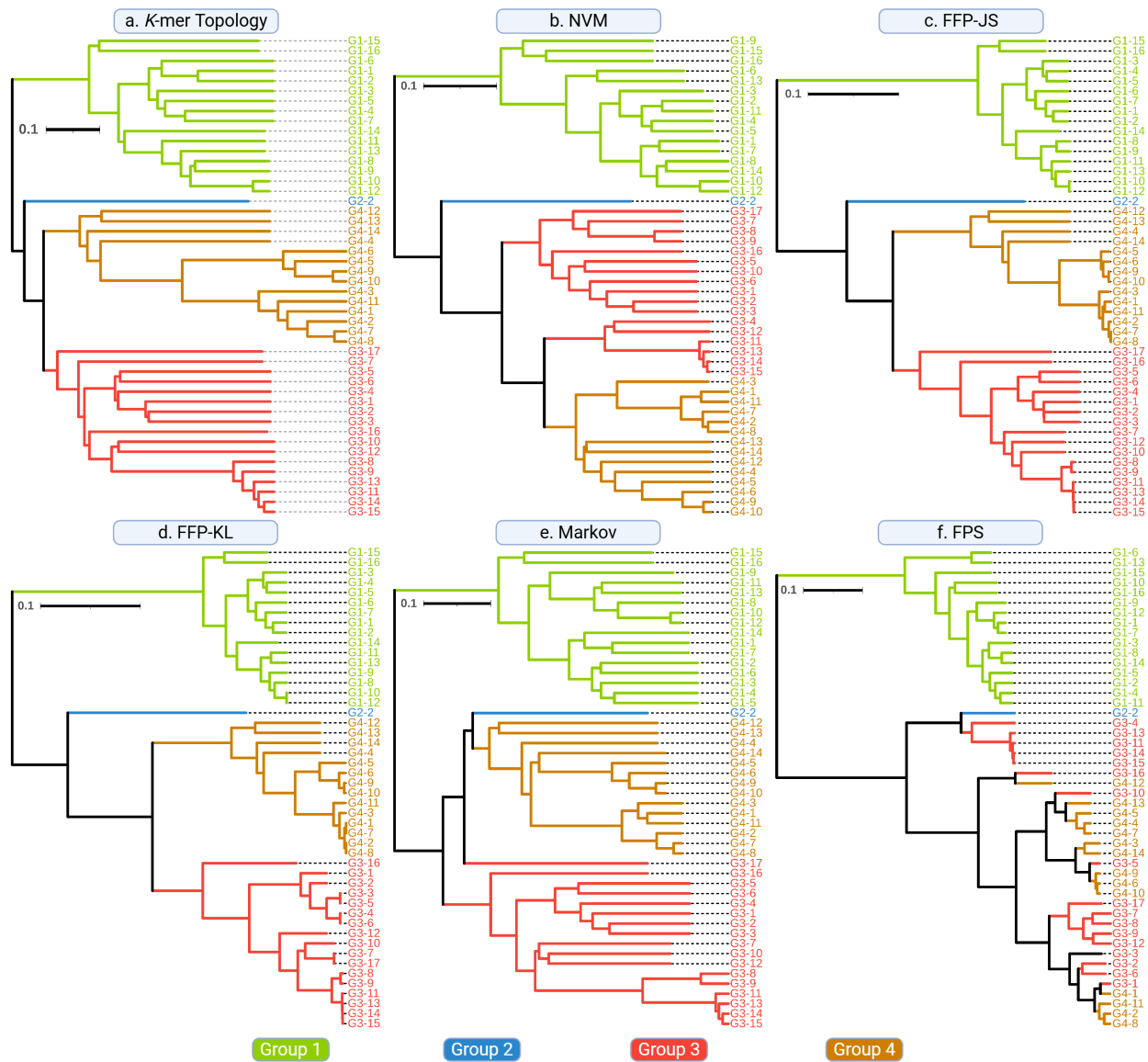


Figure S4: Phylogenetic trees of 48 complete hepatitis E virus (HEV) genomes. HEV are categorized into 4 groups: 1, 2, 3 and 4. The branches and labels are colored based on the HEV group. (a) *K*-mer topology using $k = 5$: All HEV genomes are correctly classified into their respective clades. (b) NVM using $k = 5$: HEV groups 1, 2 and 4 are correctly classified into their respective clades. Group 3 genomes are in 2 distinct clades. (c) FFP-JS using $k = 3$: All HEV genomes are correctly classified into their respective clades. (d) FFP-KL using $k = 3$: All HEV genomes are correctly classified into their respective clades. (e) Markov K-String using $k = 3$: One Group 3 genome (G3-17) is misclassified. (f) Fourier power spectrum (FPS): Only Group 1 HEV genomes are clustered together. The other groups do not form cohesive clades.

S3.2 Influenza A hemagglutinin genes

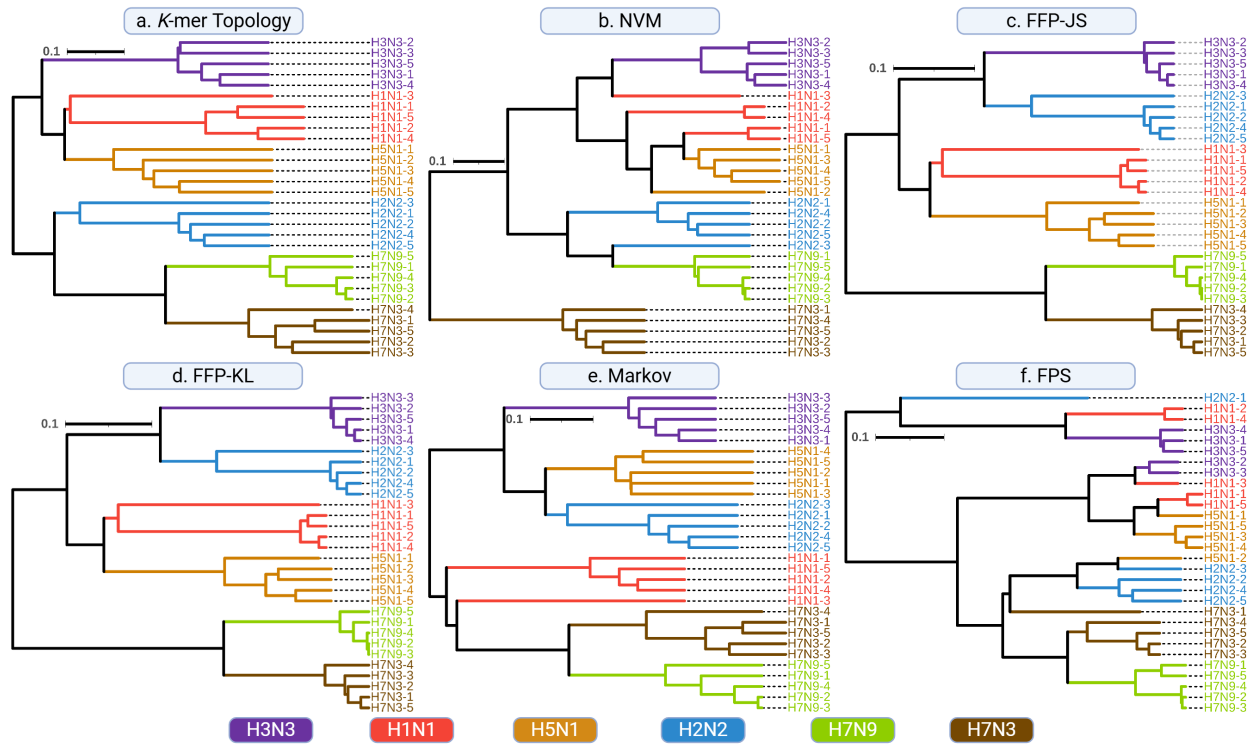


Figure S5: Phylogenetic trees of 30 influenza A hemagglutinin (HA) genes. Influenza HA genes are categorized into 6 groups: H1N1, H2N2, H3N2, H5N1, H7N9, and H7N3. The branches and labels are color-coded according to the influenza A classifications. (a) *K*-mer topology using $k = 3$: All influenza A HA genes are correctly classified into their respective clades. (b) NVM using $k = 3$: H1N1 HA genes do not form a clade. One H5N1 gene (H5N1-2) is misclassified. (c) FFP-JS using $k = 3$: All influenza A HA genes are correctly classified into their respective clades. (d) FFP-KL using $k = 3$: All influenza A HA genes are correctly classified into their respective clades. (e) Markov *K*-String using $k = 3$: One H1N1 gene (H1N1-3) is misclassified. (f) Fourier power spectrum (FPS): Only the H7N9 HA genes form a clade.

S3.3 Ebola virus

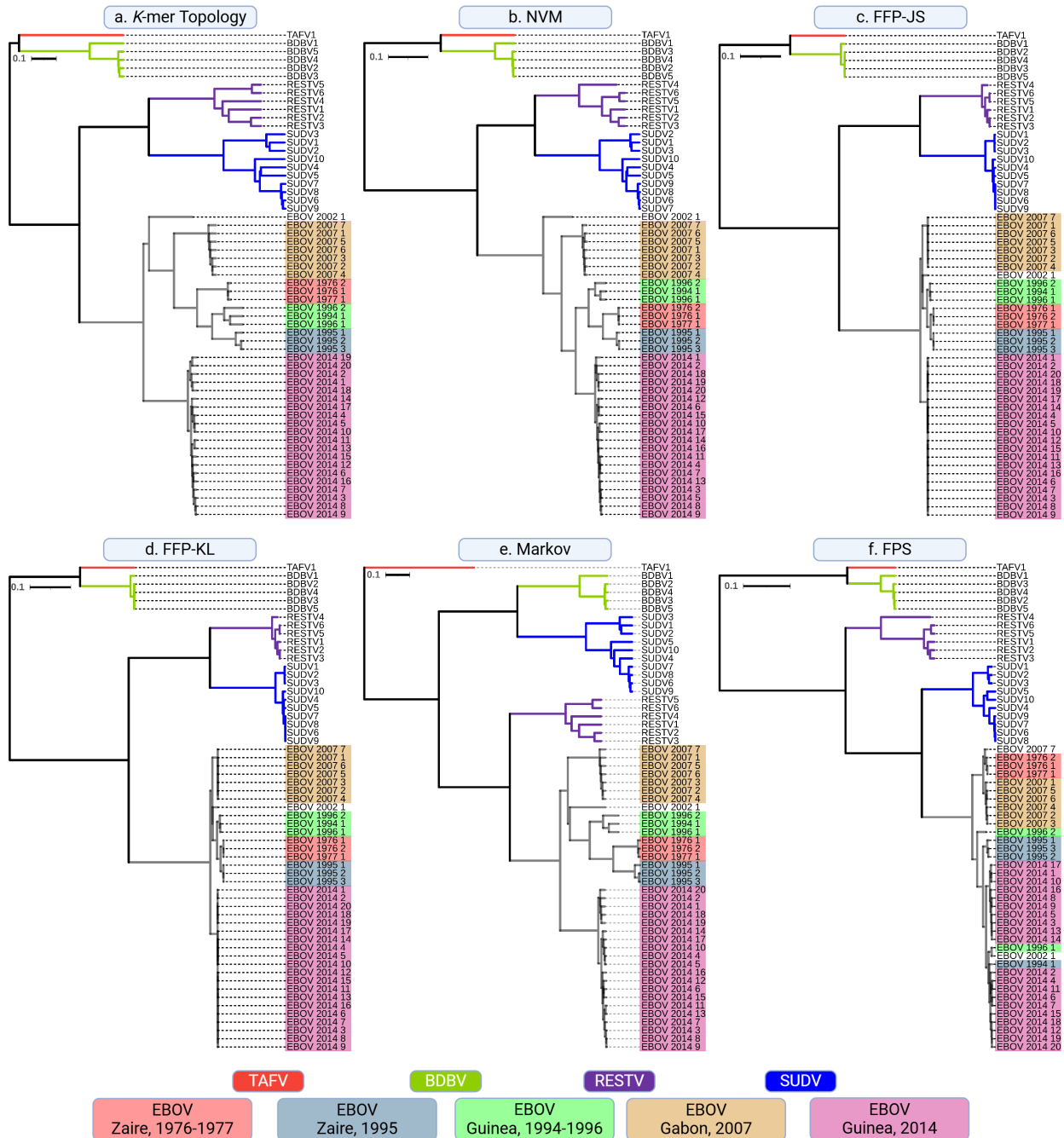


Figure S6: Phylogenetic trees of 59 complete ebola virus genomes. Ebolaviruses are categorized into five types: Bundibugyo virus (BDBV), Reston virus (RESTV), Ebola virus (EBOV), Sudan virus (SUDV), and Tai Forest virus (TAFV). EBOV is further subdivided based on epidemic location and year. The branches are colored based on the ebola virus types, and the labels are highlighted according to its EBOV epidemic. (a) *K*-mer topology using $k = 5$: All ebola virus genomes are correctly classified into their respective clades, with EBOV epidemics also clustered within the clades. (b) NVM using $k = 5$: All ebola virus genomes are correctly classified into their respective clades, with EBOV epidemics also clustered within the clades. (c) FFP-JS using $k = 3$: All ebola virus genomes are correctly classified into their respective clades, with EBOV epidemics also clustered within the clades. (d) FFP-KL using $k = 3$: All ebola virus genomes are correctly classified into their respective clades, with EBOV epidemics also clustered within the clades. (e) Markov K-String using $k = 3$: All ebola virus genomes are correctly classified into their respective clades, with EBOV epidemics also clustered within the clades. (f) Fourier power spectrum (FPS): All ebola virus genomes are correctly classified into their respective clades; however, EBOV epidemics are not clustered together.

S3.4 Bacteria

Figure S7 compares k -mer topology with five other methods on the whole bacteria genome data. The dataset contains 30 sequences, categorized into nine families. The label colors correspond to each family.

All methods cluster each family into a separate clade; however, their divisions show significant differences.

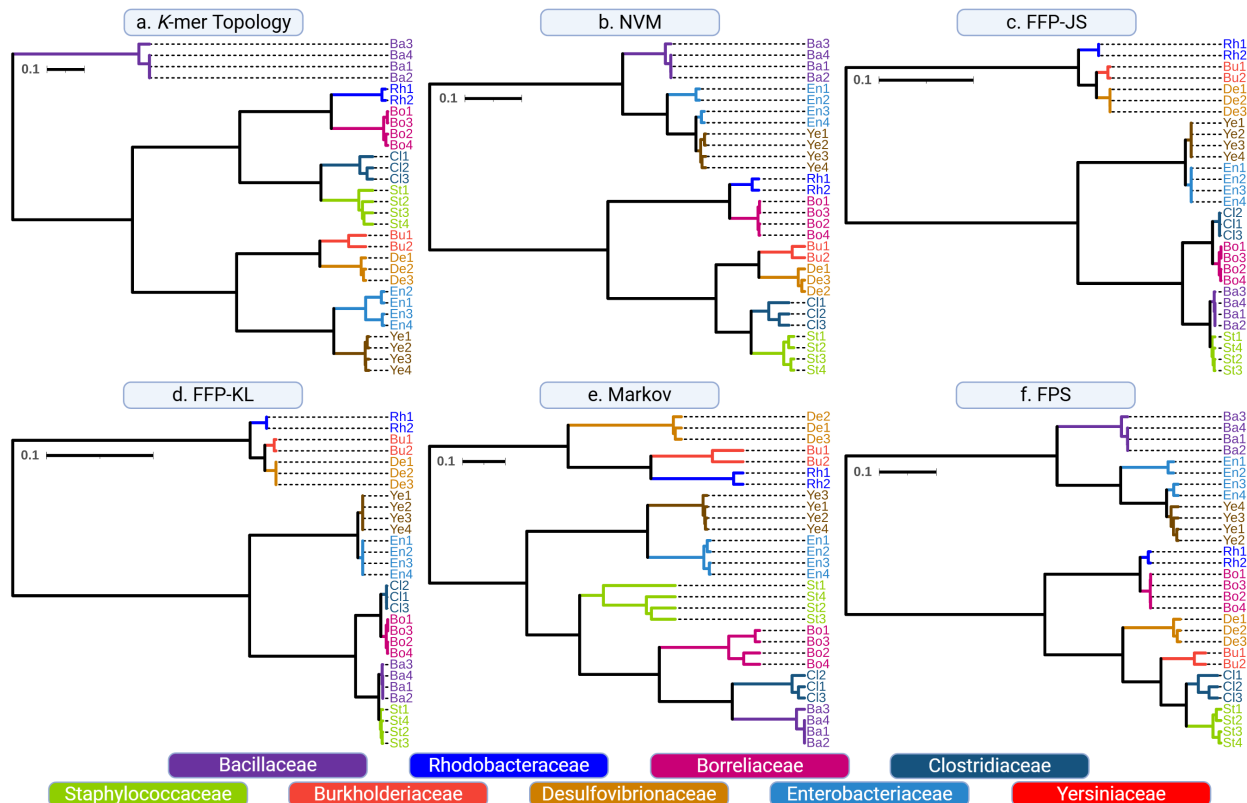


Figure S7: Phylogenetic trees of influenza A hemagglutinin (HA) genes generated using (a) K -mer Topology with $K = 5$, (b) NVM with $k = 7$, (c) FFP-JS, (d) FFP-KL, (e) Markov K-String, and (f) FPS. The labels and clades are colored according to their types.

S4 Distribution of k -mers

K -mer based methods often calculate the statistics on the frequency of the individual k -mers but do not take into account the local distribution of the individual k -mer. For example, NVM takes positional information into account and calculates statistics on the distribution, such as the average position, the variance of the positions, and more. However, local structural information is not considered.

Figure S8 shows the local distribution of each k -mer type. For a given k -mer type, we count how many k -mers of the same type exist within a distance of r and then take the average. In Figure S8, we calculated the distribution for the 16 possible 2-mer types in eight different viral families in the NCBI reference data. We can see that different sequences (or species) exhibit different local distributions. For example, *Phenuviridae* exhibits a high local average frequency of TCs, whereas they show a very low local average frequency of CG. These local distributions are not taken into account in the other existing k -mer-based methods, which motivates the use of k -mer topology for a more detailed analysis of this local structural information.

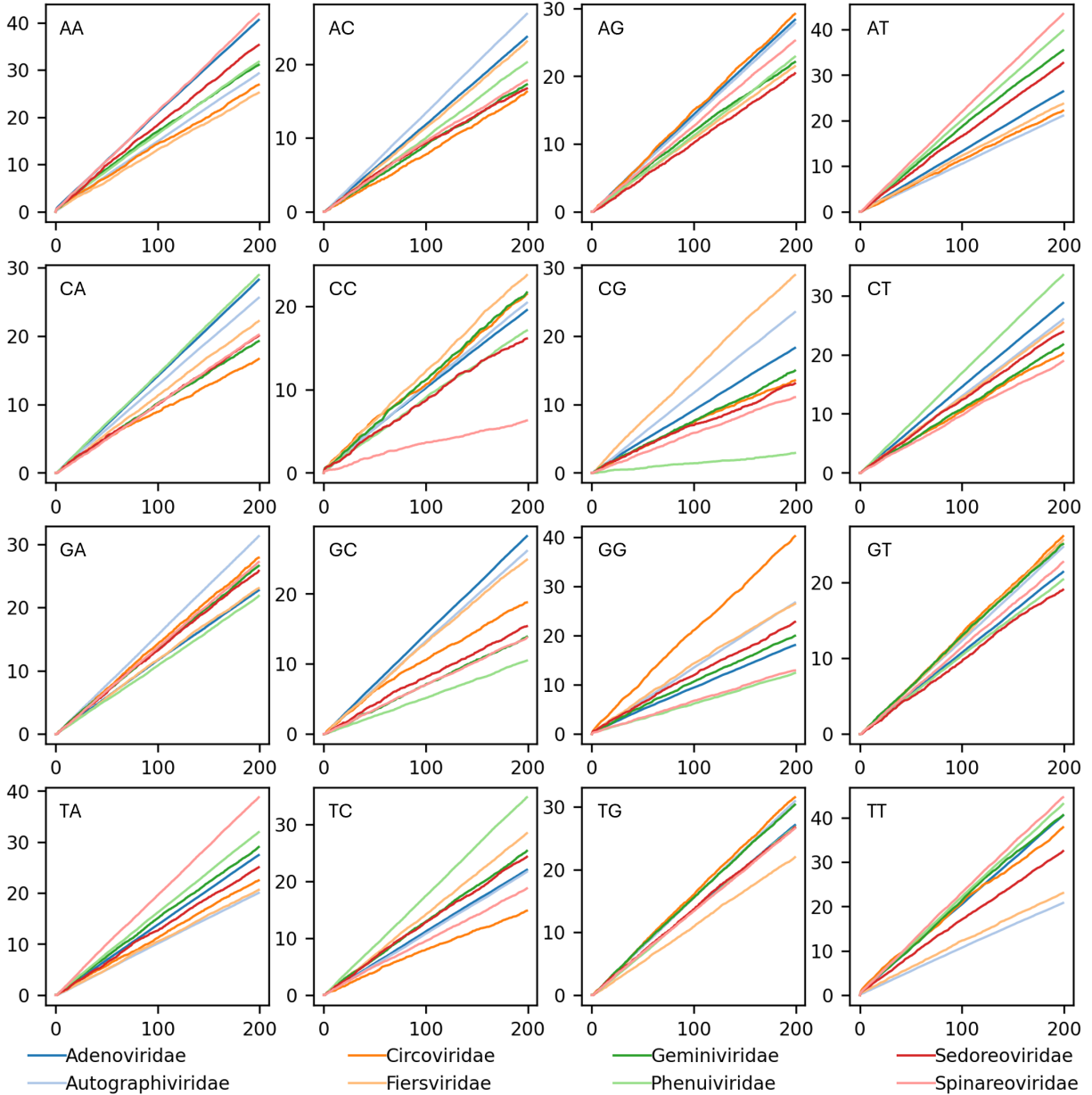


Figure S8: Distribution of 2-mers of 8 viral families: AC.000001.1 (*Adenoviridae*) NC.001271.1 (*Autographiviridae*) NC.001792.2 (*Circoviridae*) NC.001417.2 (*Fiersviridae*) NC.000869.1 (*Geminiviridae*) NC.002323.1 (*Phenuiviridae*) NC.003760.1 (*Sedoreoviridae*) NC.002557.1 (*Spinareoviridae*). Each plot corresponds to one of 16 2-mer types, and the lines are colored according to their families. The x -axis and y -axis correspond to the radius and averaged 2-mer counts.

S5 Persistent Laplacian improves persistent homology in phylogenetic analysis

Persistent homology provides persistent Betti numbers [39, 48] that can facilitate the first term in our topological genetic distance, Eq. (S1). The k -mer topology utilizes only persistent Betti numbers is termed persistent homology-based k -mer topology. However, persistent homology has many limitations [42, 58]. Persistent Laplacians outperform persistent homology in protein engineering [59]. Therefore, the k -mer

topology is proposed based on persistent Laplacians and is referred to the persistent Laplacian-based k -mer topology. In this case, both persistent Betti numbers and non-harmonic persistent eigenvalues are used. For most datasets studied in this work, the persistent homology-based k -mer topology works well. However, the phylogenetic analysis of SARS-CoV-2 variants is a very challenging case, for which all other existing methods do not work well. Figure S9 shows that the persistent homology-based k -mer topology encounters difficulty for the phylogenetic analysis of SARS-CoV-2 variants. However, the persistent Laplacian-based k -mer topology improves the phylogenetic analysis of the persistent homology-based k -mer topology and achieves fully correct phylogenetic genetic clustering.

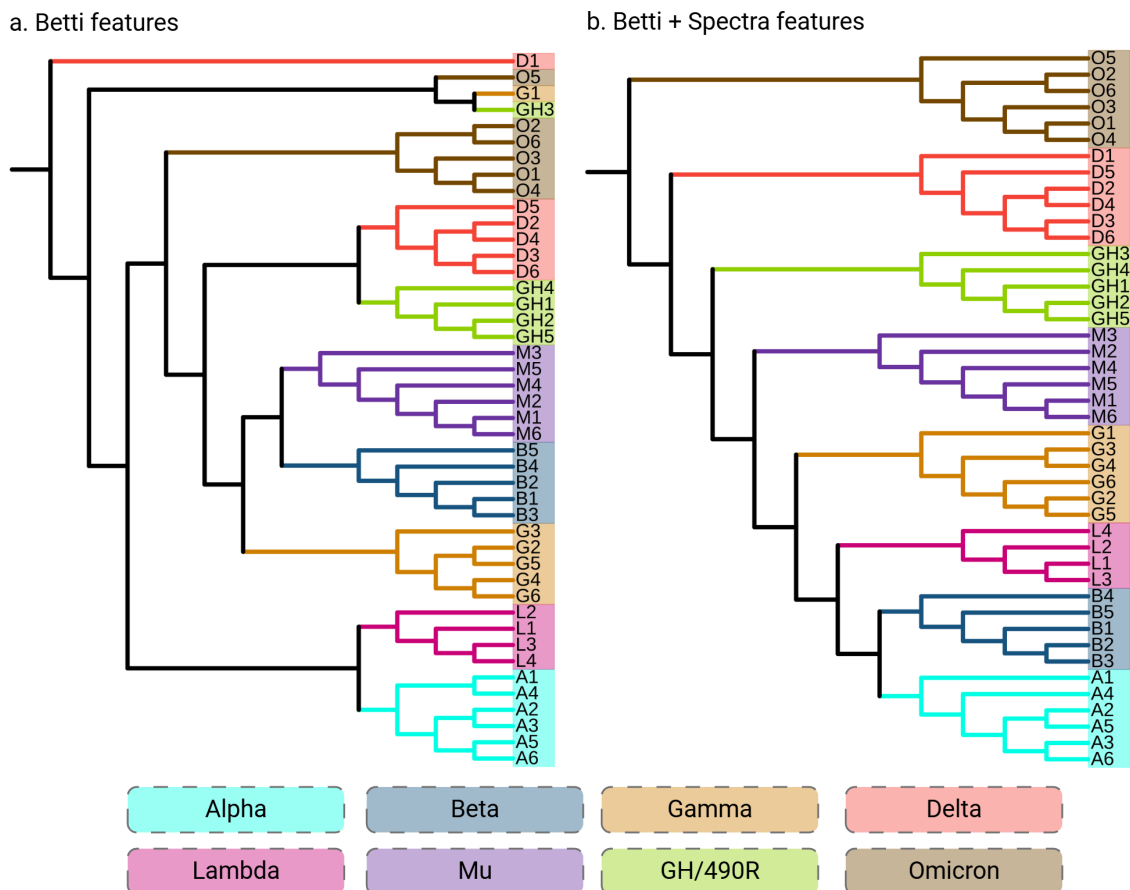


Figure S9: Comparison of persistent Laplacian-based and persistent homology-based phylogenetic trees of whole SARS-CoV-2 genomes. The clades are colored according to the SARS-CoV-2 variants, and the labels are the accession ID from GISAID. (a) Phylogenetic tree generated from persistent homology. Four sequences—D1, O5, GH3, and G1—are misclassified. All other sequences are clustered within their respective clades. (b) Phylogenetic tree generated from persistent Laplacians, including the Betti numbers and the smallest non-zero eigenvalue. All sequences are corrected clustered.

S6 Further analysis of persistent Laplacian on DNA sequences

Figure S10 shows the comparison between H1N1 using the standard persistent Laplacian (Figure S10(a)) and the circular persistent Laplacian (Figure S10(b)). In the circular Laplacian, the 5' and 3' ends are glued together to form a loop. A 2-mer AC was used to compare the two methods.

Not surprisingly, when we consider the sequence as a circle, the local AC count increases. Additionally, Betti-0 decreases faster for the circular sequence. Most interestingly, we observe a significant difference between the spectral curves. For the standard case, the spectral curve gradually increases from $r = 40$, while

in the circular case the growth is much faster, nearly tripling the value by $r = 200$. In the circular case, the connectivity of the sequence is much higher, as the 5' end is connected with the 3' end.

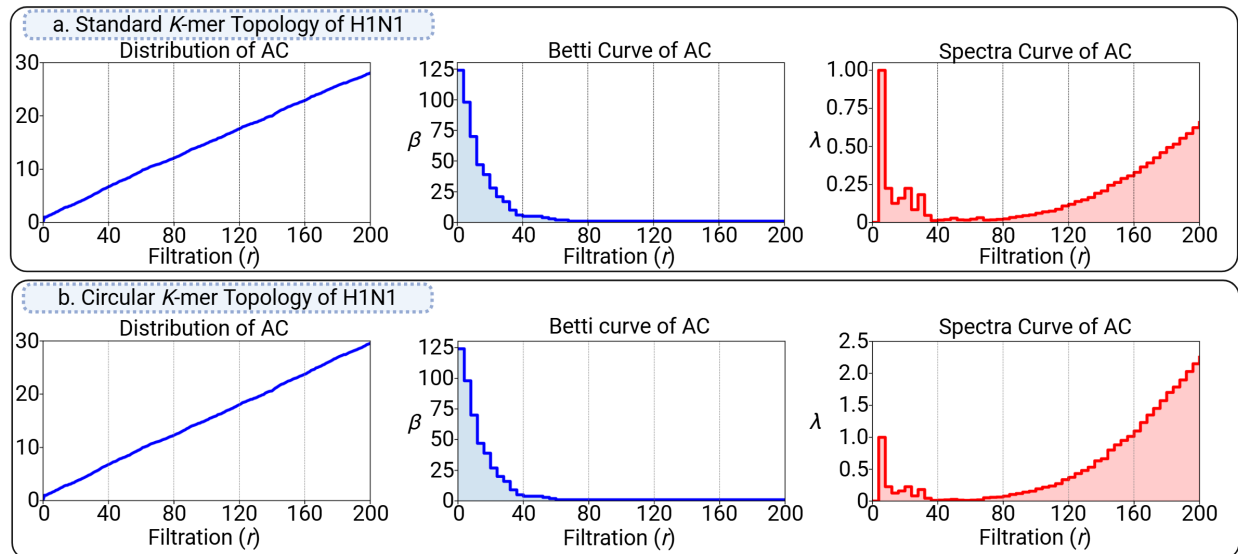


Figure S10: Comparison of the standard k -mer topology (a) and circular k -mer topology (b) using the H1N1 HA gene sequence. The left figure shows the distribution of 2-mers AC across the filtration radius. Middle figure shows the Betti-0 curve of AC. The right figure shows the smallest nonzero eigenvalue across different filtration radius.

S7 Further details on the codes used in comparisons

This work reproduced all the codes of the methods used in the comparisons. Specifically, the natural vector method (NVM) was reproduced on the basis of [44]. Jensen-Shannon (JS) and Kullback-Leibler (KL) divergences were calculated by first calculating the feature frequency profiles (FFPs), which are the normalized k -mer counts. The JS and KL divergences are calculated by treating the FFPs as a probability distribution. More details can be found in [16, 26, 45]. Markov K-String method was reproduced on the basis of [46]. The code for the Fourier power spectrum (FPS) was given in the original work [35] and is available on the Mathworks' website <http://www.mathworks.com/matlabcentral/fileexchange/49026m>. The codes we reproduced (i.e., NVM, FFP-JS, FFP-KL, FPS) can be found at <https://github.com/hozumiyu/PhyloBenchmark>

S8 Classification data

Table S3 shows the overview of the dataset used for our viral classification task. For NCBI 2020 and NCBI 2022, we utilized the dataset from Sun et al. [44] and Yu et al. [63], respectively. Since some reference sequences from NCBI 2020 and NCBI 2022 were removed from the NCBI viral database, we removed these sequences. Additionally, some viral sequences have different taxonomy from the most recent classification, but we utilized the original taxonomy from the studies. For the NCBI 2024 dataset, we obtained the sequences from the NCBI viral database, which was accessed on January 20, 2024. For all the dataset, we removed any viral family which only had 1 reference sequence.

Table S3: Dataset, NCBI collection date, preprocessing procedure, number of families and number of sequences

Name	NCBI date	Removed sequence	# families	# sequence
NCBI 2020 [44]	03/2020	Unknown Baltimore class Unknown family families <2 sequence	83	6,993
NCBI 2022 [63]	03/2022	Partial sequence Unknown family families <2 sequence Invalid nucleotides	123	11,428
NCBI 2024	01/20/2024	Partial sequence Unknown family Only '-viridae' families <2 sequence Invalid nucleotide	199	12,154
NCBI 2024 full	01/20/2024	Partial sequence Unknown family families <2 sequence	209	13,645

S9 Phylogenetic analysis data

In this section, we present the description of each dataset used for the phylogenetic analysis.

Table S5: Viral family name, number of sequence, minimum, maximum and average sequence length, and average N_A , N_C , N_G , N_T

Family	# sequence	Min length	Max length	Avg length	Avg N_A	Avg N_C	Avg N_G	Avg N_T
Ackermannviridae	64	143249.00	167619.00	156691.41	42614.16	35865.44	36011.62	42200.19
Adenoviridae	124	415.00	48395.00	31944.69	8050.70	8074.22	8017.19	7802.57
Adintoviridae	2	12571.00	12754.00	12662.50	3797.50	2582.50	2572.50	3710.00
Aliceevansviridae	129	30664.00	48800.00	36318.58	12465.62	6405.73	7710.43	9736.81
Aliusviridae	8	13163.00	15277.00	14150.62	4418.38	2773.00	2861.50	4097.75
Alloherpesviridae	17	451.00	295146.00	135007.88	32656.82	34600.47	34880.06	32870.53
Allomimiviridae	2	186217.00	668031.00	427124.00	128975.00	84000.00	86135.00	128014.00
Alphaflexiviridae	67	762.00	8831.00	6742.87	1897.00	1938.70	1435.27	1471.90
Alphasatellitidae	122	619.00	1531.00	1270.06	385.78	239.97	291.65	352.66
Alphatetraviridae	8	2055.00	6625.00	4027.88	919.62	1195.38	1024.00	888.88
Alternaviridae	24	1420.00	3594.00	2710.62	506.08	660.92	843.17	700.46
Amalgaviridae	23	3156.00	3478.00	3389.30	865.65	721.48	918.78	883.39
Amesuviridae	3	2707.00	3442.00	2952.00	764.00	597.00	747.33	843.67
Amnoonviridae	10	465.00	1641.00	1032.00	260.60	263.10	217.10	291.20
Ampullaviridae	3	22609.00	28489.00	24970.00	8106.67	4104.00	4158.00	8601.33
Anelloviridae	174	1744.00	3907.00	2739.02	860.40	668.24	601.16	609.22
Arenaviridae	131	1924.00	7417.00	5027.60	1436.51	1088.17	952.91	1550.02
Arteriviridae	25	12704.00	15728.00	14978.60	3342.24	4098.16	3634.80	3903.40
Artoviridae	8	6367.00	12395.00	10072.50	2959.00	2227.88	2130.12	2755.50
Ascoviridae	8	741.00	199721.00	129876.00	35897.38	28953.75	29567.75	35457.12
Asfarviridae	20	170101.00	193886.00	184524.00	56550.50	35563.90	35537.35	56872.25
Aspiviridae	14	136.00	8182.00	3002.50	823.86	613.07	449.71	1115.86
Assiduviridae	3	53385.00	57447.00	54832.00	21130.00	7363.33	9868.00	16470.67
Astroviridae	59	2403.00	7722.00	5978.46	1621.12	1416.78	1453.34	1487.22
Atkinsviridae	91	3364.00	4535.00	3895.51	919.65	947.07	975.75	1053.04
Autographiviridae	385	10313.00	47868.00	41458.66	10671.61	10054.84	10850.82	9881.40
Autolykiviridae	5	10046.00	10636.00	10428.80	3035.00	2268.20	2251.60	2874.00
Avsunviroidae	5	247.00	434.00	350.00	79.40	89.20	90.40	91.00
Bacilladnaviridae	21	3492.00	6000.00	4955.76	1285.00	1164.71	1067.43	1438.62
Baculoviridae	103	1182.00	178733.00	127394.97	37115.49	26505.71	26608.93	37164.84
Benyviridae	15	1320.00	7038.00	4319.27	1076.07	782.27	1103.60	1357.33
Betaflexiviridae	151	276.00	9654.00	7604.56	2223.48	1457.15	1847.44	2076.48
Bicaudaviridae	8	48774.00	76107.00	62491.50	19691.50	12002.00	11801.88	18996.12
Bidnaviridae	4	6022.00	6543.00	6283.00	2263.25	915.75	968.50	2135.50
Birnaviridae	29	2605.00	3579.00	3076.34	911.93	838.45	751.72	574.24

Table S6: Viral family name, number of sequence, minimum, maximum and average sequence length, and average N_A , N_C , N_G , N_T

Family	# sequence	Min length	Max length	Avg length	Avg N_A	Avg N_C	Avg N_G	Avg N_T
Blumeviridae	34	3612.00	4744.00	4247.59	1104.85	959.65	994.06	1189.03
Bornaviridae	19	5572.00	9006.00	8730.74	2493.58	1864.32	1933.11	2439.74
Botourmiaviridae	165	958.00	5234.00	2607.88	602.54	623.37	723.52	658.45
Bromoviridae	125	1938.00	3644.00	2791.70	754.28	557.18	663.09	817.16
Caliciviridae	55	6434.00	8513.00	7633.36	1955.00	1995.89	1882.18	1800.29
Casjensviridae	60	54417.00	63971.00	59167.30	12699.53	16831.58	16886.03	12750.15
Caulimoviridae	111	545.00	13221.00	7557.92	2622.24	1483.11	1622.64	1829.93
Chaacviridae	3	10198.00	10798.00	10590.33	3120.33	2099.00	2131.00	3240.00
Chaseviridae	30	50725.00	57429.00	53436.43	14847.23	11713.60	12712.93	14162.67
Chrysoviridae	124	646.00	4220.00	2993.94	797.73	654.73	868.04	673.44
Chuviridae	52	1566.00	12996.00	8314.12	2338.31	1877.65	1924.63	2173.52
Circoviridae	283	648.00	4706.00	2075.54	558.73	463.52	486.42	566.87
Closteroviridae	80	555.00	19296.00	12470.34	3612.10	2363.55	2832.50	3662.19
Coronaviridae	74	25423.00	36549.00	28649.42	7734.05	5136.28	6183.97	9595.11
Corticoviridae	2	10079.00	10584.00	10331.50	3266.00	1876.00	2466.50	2723.00
Cretegaviridae	2	14939.00	17738.00	16338.50	4477.50	3937.50	3404.00	4519.50
Crevaviridae	4	83412.00	95815.00	91473.00	31640.50	13642.75	14205.25	31984.50
Cruliviridae	9	799.00	6691.00	3675.33	1189.33	681.00	757.44	1047.56
Curvulaviridae	16	1634.00	2383.00	2027.12	470.00	543.12	581.94	432.06
Cystoviridae	21	2322.00	7051.00	4507.38	961.29	1264.67	1248.33	1033.10
Deltaflexiviridae	4	6735.00	8327.00	7871.50	1521.00	2301.25	1804.00	2245.25
Demereciviridae	101	14504.00	128602.00	113646.65	34213.77	22765.17	22759.50	33908.22
Dicistroviridae	28	7835.00	10436.00	9329.18	2832.18	1725.96	1923.82	2847.21
Discoviridae	15	1091.00	6519.00	2913.00	822.00	632.00	605.80	853.20
Drexlerviridae	119	37655.00	54438.00	49347.62	13424.13	11270.55	11725.51	12927.43
Druskaviridae	3	102105.00	103257.00	102560.33	21843.67	29221.00	29859.33	21636.33
Duinviridae	6	3543.00	4458.00	3888.17	1056.50	856.00	857.67	1118.00
Duneviridae	6	39290.00	46976.00	43646.83	13859.67	7272.33	6520.83	15994.00
Endornaviridae	40	9636.00	23635.00	14493.67	4893.88	2786.15	3240.93	3572.72
Euroniviridae	3	24648.00	29384.00	26283.33	8126.00	5842.00	5691.33	6624.00
Fiersviridae	302	3211.00	5067.00	3793.80	896.41	941.81	971.92	983.67
Filoviridae	16	13065.00	19114.00	17376.69	5269.31	3885.31	3696.38	4525.69
Fimoviridae	159	980.00	7291.00	2512.94	853.79	395.53	380.10	883.52
Flaviviridae	169	1011.00	22780.00	9855.40	2614.54	2242.76	2723.79	2274.31
Forsetiviridae	2	43978.00	47186.00	45582.00	18538.00	5287.00	7861.50	13895.50

Table S7: Viral family name, number of sequence, minimum, maximum and average sequence length, and average N_A , N_C , N_G , N_T

Family	# sequence	Min length	Max length	Avg length	Avg N_A	Avg N_C	Avg N_G	Avg N_T
Fredfastierviridae	3	43365.00	43783.00	43546.00	11601.67	9808.00	9856.67	12279.67
Fusariviridae	38	3253.00	10776.00	6847.63	1832.16	1504.05	1641.18	1870.24
Fuselloviridae	10	14796.00	24186.00	16690.30	5161.00	3134.30	3384.70	5010.30
Gammaflexiviridae	4	6827.00	9525.00	8223.50	1773.75	3008.75	1702.25	1738.75
Geminiviridae	816	2383.00	3763.00	2701.93	704.61	556.02	630.00	811.30
Genomoviridae	254	1309.00	2826.00	2190.00	550.62	594.52	532.52	512.35
Globuloviridae	4	18212.00	28332.00	21530.50	5177.00	4946.75	5759.00	5647.75
Graaviviridae	2	39784.00	42271.00	41027.50	7176.00	13421.00	13244.00	7186.50
Grimontviridae	10	75106.00	112127.00	89328.00	26681.40	18199.10	17223.20	27224.30
Guelinviridae	10	16747.00	19089.00	18297.50	6461.20	2699.30	2991.20	6145.80
Hadakaviridae	11	859.00	2539.00	1394.00	362.36	277.36	375.27	379.00
Hafunaviridae	12	56593.00	77672.00	71940.17	14879.92	20533.17	20770.33	15756.75
Haloferuviridae	3	35722.00	38059.00	36794.67	8789.00	10094.00	11266.33	6645.33
Hantaviridae	147	324.00	6761.00	3772.86	1213.63	638.73	807.94	1112.56
Hepadnaviridae	26	3018.00	3542.00	3189.00	808.35	818.15	681.96	880.54
Hepeviridae	13	6555.00	7312.00	6955.77	1444.23	1958.08	1796.38	1757.08
Herelleviridae	137	203.00	167431.00	138558.36	46349.77	23727.21	26266.80	42214.58
Hypoviridae	40	7381.00	18371.00	12286.15	3218.18	2941.85	3035.75	3090.38
Hytrosaviridae	2	124279.00	190032.00	157155.50	52546.00	26344.00	27304.00	50961.50
Iflaviridae	46	8832.00	10984.00	9939.28	2954.98	1755.46	2138.98	3089.87
Inoviridae	74	4772.00	10638.00	7006.72	1571.51	1721.42	1828.30	1885.49
Intestiviridae	18	89781.00	98001.00	93488.00	32712.94	13910.39	14324.56	32540.11
Iridoviridae	29	1392.00	288858.00	156330.21	48320.34	30163.24	30486.34	47360.28
Kitaviridae	29	1724.00	8893.00	5135.69	1319.86	987.28	1149.48	1679.07
Kleczkowskaviridae	2	206821.00	207623.00	207222.00	61537.50	40014.50	45177.00	60493.00
Kolmioviridae	15	1547.00	1735.00	1663.87	355.87	480.47	463.87	363.67
Kyanoviridae	76	144311.00	252401.00	185396.74	56901.86	35163.88	39096.28	54234.72
Lavidaviridae	6	17276.00	29767.00	22079.83	7568.17	3639.33	3706.00	7166.33
Leishbuviridae	3	661.00	5981.00	2607.33	834.33	485.33	525.67	762.00
Leisingerviridae	2	26111.00	31007.00	28559.00	8541.00	5858.00	7279.50	6880.50
Lipothrixviridae	10	31324.00	41171.00	37568.10	11729.40	7071.30	6635.40	12132.00
Lispiviridae	30	6450.00	15623.00	11702.17	3870.67	2162.03	2244.40	3425.07
Malacoherpesviridae	2	207439.00	211518.00	209478.50	60403.00	44491.00	45137.50	59447.00
Marnaviridae	21	6360.00	9562.00	8794.62	2442.52	1824.29	1916.95	2610.86
Marseilleviridae	14	3538.00	380011.00	225563.14	63226.64	49179.79	49347.43	63809.29

Table S8: Viral family name, number of sequence, minimum, maximum and average sequence length, and average N_A , N_C , N_G , N_T

Family	# sequence	Min length	Max length	Avg length	Avg N_A	Avg N_C	Avg N_G	Avg N_T
Matonaviridae	4	9621.00	9762.00	9693.75	1516.75	3502.75	3133.75	1540.50
Matshushitaviridae	2	17036.00	19604.00	18320.00	2962.50	5869.50	6381.50	3106.50
Mayoviridae	10	2231.00	6228.00	4078.60	1066.50	810.10	989.40	1212.60
Medioniviridae	2	20268.00	25068.00	22668.00	5965.00	6561.00	4558.50	5583.50
Megabirnaviridae	6	7180.00	8985.00	8294.83	1875.00	1939.00	2399.00	2081.83
Mesoniviridae	15	18939.00	20949.00	20077.87	6765.53	4325.13	3129.73	5857.47
Mesyanzhinovviridae	18	47545.00	64096.00	59816.94	11646.83	19296.67	18980.17	9893.28
Metaviridae	2	7396.00	7510.00	7453.00	2427.50	1777.50	1549.00	1699.00
Microviridae	62	4129.00	6478.00	5177.18	1386.40	1052.24	1140.34	1598.19
Mimiviridae	16	73689.00	1572370.00	1155047.19	425426.31	151712.38	153476.62	424431.88
Mitoviridae	117	2148.00	4955.00	2846.35	877.00	545.36	578.22	845.77
Molycolviridae	2	124169.00	124692.00	124430.50	41647.50	20790.00	24332.00	37661.00
Mymonaviridae	38	3744.00	11563.00	8184.76	2191.97	1847.97	1875.03	2269.79
Mypoviridae	3	2579.00	9874.00	5325.67	1838.67	893.00	1027.00	1567.00
Nairoviridae	147	1443.00	14854.00	6308.70	2036.27	1260.44	1401.37	1610.62
Nanoviridae	114	957.00	1111.00	1005.55	303.89	162.66	231.63	307.37
Narnaviridae	17	1455.00	9885.00	3557.00	928.59	794.71	848.12	985.59
Naryaviridae	3	1788.00	2085.00	1947.67	639.67	337.67	338.00	632.33
Nenyaviridae	5	1661.00	2931.00	1998.80	593.40	374.40	437.00	594.00
Nimaviridae	2	305119.00	309286.00	307202.50	92663.00	62846.00	62983.50	88710.00
Nodaviridae	30	1175.00	3628.00	2409.70	614.90	642.13	593.03	559.63
Nudiviridae	14	96944.00	231621.00	147162.79	48097.00	25620.21	25554.64	47890.93
Nyamiviridae	23	4708.00	13295.00	9909.87	2704.57	2384.57	2391.61	2429.13
Orlajensenviridae	11	17049.00	17510.00	17397.00	2918.36	6091.91	5849.09	2537.64
Orthoherpesviridae	136	165.00	241087.00	134009.69	30292.34	37057.08	36561.10	30099.18
Orthomyxoviridae	191	508.00	2427.00	1730.04	565.30	340.38	419.36	404.99
Pachyviridae	5	71443.00	78833.00	74320.00	27252.40	11124.40	12844.80	23098.40
Papillomaviridae	208	5748.00	8809.00	7597.20	2206.78	1550.24	1790.64	2049.54
Paramyxoviridae	92	14796.00	21523.00	16270.03	5203.63	3331.50	3421.03	4313.87
Partitiviridae	162	1186.00	2499.00	1890.64	507.31	518.17	346.98	518.18
Parvoviridae	227	3411.00	6334.00	4916.39	1541.87	1081.06	1094.38	1199.08
Paulinoviridae	2	5688.00	5804.00	5746.00	804.50	1541.00	1975.00	1425.50
Peduviridae	108	18281.00	40555.00	33441.85	7988.25	8852.69	9001.21	7599.69
Peribunyaviridae	451	585.00	8905.00	4090.36	1495.58	652.55	761.91	1180.32
Permutotetraviridae	3	2482.00	5698.00	4011.33	997.67	929.67	1128.33	955.67

Table S9: Viral family name, number of sequence, minimum, maximum and average sequence length, and average N_A , N_C , N_G , N_T

Family	# sequence	Min length	Max length	Avg length	Avg N_A	Avg N_C	Avg N_G	Avg N_T
Pervagoviridae	2	72534.00	72979.00	72756.50	22550.00	13838.50	13868.50	22499.50
Phasmaviridae	97	1040.00	7740.00	3818.56	1338.51	625.15	765.16	1089.73
Phenuiviridae	450	461.00	9760.00	3941.68	1214.75	766.00	869.07	1091.85
Phycodnaviridae	59	285.00	1473473.00	166979.15	51369.73	32096.90	32042.61	51469.92
Picobirnaviridae	15	1688.00	2666.00	2078.93	594.67	438.00	491.00	555.27
Picornaviridae	203	2086.00	10101.00	7799.63	2069.96	1802.47	1761.30	2165.90
Plectroviridae	6	4491.00	8273.00	7184.17	2719.50	652.83	1063.00	2748.83
Pleolipoviridae	16	7048.00	16992.00	11349.50	2556.75	3051.56	3150.88	2590.31
Pneumoviridae	10	13350.00	15225.00	14729.60	5300.40	2687.80	2704.00	4037.40
Polycipiviridae	9	10315.00	12155.00	11498.56	3680.00	2120.33	2220.22	3478.00
Polydnaviriformidae	346	263.00	140906.00	8701.72	2796.08	1567.32	1568.05	2770.28
Polymycoviridae	54	890.00	2470.00	1792.56	338.17	542.13	525.15	387.11
Polyomaviridae	142	3962.00	14334.00	5217.19	1502.44	1114.36	1091.63	1508.76
Pootjesviridae	10	143349.00	158568.00	153196.80	39322.80	37903.80	37574.90	38395.30
Portogloboviridae	2	20222.00	20424.00	20323.00	6268.00	3835.50	3974.50	6245.00
Pospiviroidae	41	246.00	396.00	329.27	66.34	95.44	94.83	72.66
Potyviridae	244	1103.00	11519.00	7962.33	2547.37	1510.59	1848.71	2055.66
Poxviridae	77	296.00	359853.00	148718.92	49760.71	24699.12	24727.68	49531.42
Qinviridae	16	1601.00	6585.00	3862.88	1007.06	978.75	998.25	878.81
Quadriviridae	4	3685.00	4942.00	4269.50	1180.25	1032.50	1222.25	834.50
Retroviridae	93	266.00	13246.00	8259.47	2455.45	1917.72	1837.30	2049.00
Rhabdoviridae	352	993.00	16133.00	11516.48	3657.11	2240.64	2506.55	3112.18
Roniviridae	4	26253.00	29110.00	27197.75	7523.75	7310.25	4804.50	7559.25
Rountreeviridae	39	16687.00	18899.00	17991.59	6121.13	2832.90	2759.10	6278.46
Rudiviridae	19	20269.00	36493.00	31298.68	11373.37	4428.95	4464.95	11031.42
Salasmaviridae	34	18379.00	28950.00	22618.79	7468.91	3849.68	3764.50	7535.71
Saparoviridae	2	52643.00	54291.00	53467.00	9617.00	17623.50	18398.00	7828.50
Sarthroviridae	8	502.00	872.00	766.88	226.50	174.00	158.12	208.25
Schitoviridae	115	59080.00	103910.00	73818.29	19903.55	17375.44	17138.30	19400.99
Schizomimiviridae	2	370920.00	1421182.00	896051.00	340731.50	107230.00	108384.50	339705.00
Secoviridae	197	229.00	13198.00	5928.11	1574.44	1179.27	1425.53	1748.87
Sedoreoviridae	458	528.00	5792.00	1865.13	586.25	339.33	434.15	505.40
Simuloviridae	3	16492.00	18925.00	17535.33	3580.67	5362.67	5671.00	2921.00
Sinhaliviridae	9	5877.00	5991.00	5910.89	1152.33	1632.56	1412.44	1713.56
Smacoviridae	88	1881.00	3028.00	2547.85	620.78	603.68	598.12	725.26

Table S10: Accession, group, sequence length of ebola virus data

Accession	Group	Length	N_A	N_C	N_G	N_T	Accession	Group	Length	N_A	N_C	N_G	N_T
FJ217161.1	BDBV	18940	5964	4324	3632	5020	KC545393.1	BDBV	18939	5974	4293	3636	5036
KC545395.1	BDBV	18939	5975	4290	3635	5039	KC545394.1	BDBV	18939	5974	4292	3637	5036
KC545396.1	BDBV	18939	5975	4293	3635	5036	FJ217162.1	TAFV	18935	6020	4371	3630	4914
AF522874.1	RESTV	18891	5937	3929	3746	5279	AB050936.1	RESTV	18890	5927	3924	3762	5277
JX477166.1	RESTV	18891	5935	3920	3755	5281	FJ621585.1	RESTV	18796	5900	3898	3747	5251
FJ621583.1	RESTV	18887	5928	3929	3767	5263	JX477165.1	RESTV	18887	5924	3929	3774	5260
FJ968794.1	SUDV	18875	5905	4034	3756	5180	KC242783.2	SUDV	18875	5911	4028	3750	5186
EU338380.1	SUDV	18875	5914	4032	3750	5179	AY729654.1	SUDV	18875	5920	4071	3732	5152
JN638998.1	SUDV	18875	5931	4059	3729	5156	KC545389.1	SUDV	18874	5924	4080	3731	5139
KC545390.1	SUDV	18874	5925	4080	3730	5139	KC545391.1	SUDV	18874	5924	4080	3731	5139
KC545392.1	SUDV	18874	5923	4081	3732	5138	KC589025.1	SUDV	18875	5921	4047	3734	5173
KC242801.1	EBOV	18959	6061	4037	3752	5109	NC_002549.1	EBOV	18959	6061	4035	3752	5111
KC242791.1	EBOV	18959	6061	4037	3752	5109	KC242792.1	EBOV	18959	6047	4052	3756	5104
KC242793.1	EBOV	18958	6043	4052	3761	5102	KC242794.1	EBOV	18959	6039	4063	3762	5095
AY354458.1	EBOV	18961	6054	4051	3747	5109	KC242796.1	EBOV	18959	6055	4049	3748	5107
KC242799.1	EBOV	18959	6054	4050	3748	5107	KC242784.1	EBOV	18958	6061	4028	3750	5119
KC242786.1	EBOV	18958	6063	4025	3749	5121	KC242787.1	EBOV	18958	6062	4025	3750	5121
KC242789.1	EBOV	18958	6062	4023	3750	5123	KC242785.1	EBOV	18958	6060	4026	3752	5120
KC242790.1	EBOV	18958	6060	4025	3751	5122	KC242788.1	EBOV	18958	6063	4032	3749	5114
KC242800.1	EBOV	18958	6042	4052	3762	5102	KM034555.1	EBOV	18950	6049	4049	3753	5099
KM034562.1	EBOV	18957	6051	4050	3756	5100	KM233039.1	EBOV	18953	6052	4051	3751	5099
KM034557.1	EBOV	18956	6052	4052	3753	5099	KM034560.1	EBOV	18952	6050	4051	3752	5099
KM233050.1	EBOV	18956	6053	4050	3753	5100	KM233053.1	EBOV	18957	6053	4051	3753	5100
KM233057.1	EBOV	18954	6052	4052	3751	5099	KM233063.1	EBOV	18955	6053	4052	3751	5099
KM233072.1	EBOV	18949	6049	4049	3752	5099	KM233110.1	EBOV	18956	6053	4053	3752	5098
KM233070.1	EBOV	18959	6055	4052	3753	5099	KM233099.1	EBOV	18953	6052	4052	3751	5098
KM233097.1	EBOV	18953	6051	4052	3752	5098	KM233109.1	EBOV	18958	6053	4055	3753	5097
KM233096.1	EBOV	18953	6054	4049	3751	5099	KM233103.1	EBOV	18950	6051	4050	3751	5098
KJ660346.2	EBOV	18959	6053	4052	3755	5099	KJ660347.2	EBOV	18959	6054	4052	3754	5099
KJ660348.2	EBOV	18959	6055	4051	3754	5099							

Table S4: Accession, group, sequence length of mammalian mitochondria data

Accession	Groups	Length	N_A	N_C	N_G	N_T
V00662.1	Primates	16569	5123	5176	2176	4094
D38116.1	Primates	16563	5189	5084	2104	4186
D38113.1	Primates	16554	5154	5099	2133	4168
D38114.1	Primates	16364	5059	5022	2160	4123
X99256.1	Primates	16472	5039	5231	2256	3946
Y18001.1	Primates	16521	5195	5047	2169	4110
AY863426.1	Primates	16389	5243	4953	2049	4137
D38115.1	Primates	16389	5007	5317	2168	3897
NC_002083.1	Primates	16499	5031	5403	2176	3889
NC_002764.1	Primates	16586	5306	5027	2116	4137
U20753.1	Carnivore	17009	5543	4454	2406	4606
U96639.2	Carnivore	16727	5290	4267	2366	4804
EU442884.2	Carnivore	16774	5293	4265	2398	4812
EF551003.1	Carnivore	16990	5418	4513	2478	4581
EF551002.1	Carnivore	16964	5397	4508	2467	4592
DQ402478.1	Carnivore	16868	5270	4285	2601	4712
AF303110.1	Carnivore	17020	5258	4355	2676	4731
AF303111.1	Carnivore	17017	5253	4346	2692	4726
EF212882.1	Carnivore	16805	5338	4000	2518	4949
AJ002189.1	Artiodactyla	16680	5790	4384	2210	4296
AF010406.1	Artiodactyla	16616	5594	4289	2181	4552
AF533441.1	Artiodactyla	16640	5569	4313	2189	4569
V00654.1	Artiodactyla	16338	5460	4237	2198	4443
AY488491.1	Artiodactyla	16355	5421	4298	2261	4375
NC_007441.1	Artiodactyla	16498	5542	4358	2164	4434
NC_008830.1	Artiodactyla	16719	5786	4340	2222	4371
NC_010640.1	Artiodactyla	16524	5519	4404	2205	4396
X72204.1	Cetacea	16402	5374	4527	2140	4361
NC_005268.1	Cetacea	16390	5354	4609	2162	4265
NC_001321.1	Cetacea	16398	5359	4474	2182	4383
NC_005270.1	Cetacea	16412	5374	4626	2153	4259
NC_005275.1	Cetacea	16324	5377	4525	2040	4382
NC_006931.1	Cetacea	16386	5357	4573	2164	4292
NC_001788.1	Perissodactyla	16670	5394	4819	2198	4259
X97336.1	Perissodactyla	16829	5663	4630	2131	4405
Y07726.1	Perissodactyla	16832	5623	4707	2169	4333
NC_001640.1	Perissodactyla	16660	5358	4754	2236	4312
AJ238588.1	Rodentia	16507	5301	4041	2071	5094
AJ001562.1	Rodentia	16602	5386	3913	2096	5207
AJ001588.1	Lagomorpha	17245	5429	4584	2350	4882
X88898.2	Erinaceomorpha	17447	5937	3503	2185	5822

Table S11: Accession, group, sequence length of rhinovirus data

Accession	Group	Length	N_A	N_C	N_G	N_T	Accession	Group	Length	N_A	N_C	N_G	N_T
AF499637.1	HEV	7458	2243	1677	1662	1876	AF546702.1	HEV	7406	2209	1649	1681	1867
AY751783.1	A	7137	2348	1362	1428	1999	DQ473485.1	B	7208	2338	1436	1443	1991
DQ473486.1	B	7216	2381	1428	1431	1976	DQ473488.1	B	7214	2382	1456	1447	1929
DQ473489.1	B	7223	2365	1476	1463	1919	DQ473490.1	B	7212	2362	1417	1420	2013
DQ473491.1	A	7145	2301	1383	1454	2007	DQ473492.1	A	7140	2297	1371	1443	2029
DQ473493.1	A	7134	2370	1287	1442	2035	DQ473494.1	A	7120	2389	1314	1437	1980
DQ473496.1	A	7106	2363	1342	1389	2012	DQ473497.1	A	7025	2309	1322	1396	1998
DQ473499.1	A	7123	2333	1301	1427	2062	DQ473500.1	A	7135	2336	1344	1409	2046
DQ473504.1	A	7143	2253	1380	1402	2108	DQ473505.1	A	7141	2247	1404	1409	2081
DQ473506.1	A	7149	2415	1349	1412	1972	DQ473507.1	A	7143	2407	1350	1426	1960
DQ473508.1	A	7148	2371	1389	1390	1998	DQ473510.1	A	7137	2406	1313	1424	1994
DQ473511.1	A	7036	2367	1288	1386	1995	EF077279.1	C	6944	2176	1503	1509	1756
EF077280.1	C	7015	2153	1550	1500	1812	EF173414.1	A	7125	2369	1310	1403	2043
EF173415.1	A	7124	2299	1396	1416	2013	EF173420.1	B	7219	2356	1500	1477	1886
EF173423.1	B	7216	2384	1456	1407	1969	EF173425.1	B	7215	2426	1412	1432	1944
EF186077.2	C	7134	2296	1549	1520	1769	EF582385.1	C	7099	2195	1565	1473	1866
EF582386.1	C	7114	2304	1492	1480	1838	EF582387.1	C	7086	2261	1533	1513	1779
FJ445111.1	A	7137	2388	1284	1388	2074	FJ445112.1	B	7212	2402	1391	1417	2002
FJ445113.1	A	7108	2376	1387	1407	1938	FJ445114.1	A	7134	2375	1329	1428	2002
FJ445115.1	A	7133	2377	1321	1426	2009	FJ445116.1	A	7140	2298	1356	1437	2049
FJ445117.1	A	7143	2321	1352	1421	2049	FJ445118.1	A	7119	2386	1340	1423	1970
FJ445119.1	A	7135	2354	1310	1421	2048	FJ445121.1	A	7134	2376	1328	1403	2026
FJ445122.1	A	7129	2327	1369	1445	1971	FJ445123.1	A	7126	2358	1277	1399	2091
FJ445124.1	B	7211	2403	1397	1413	1996	FJ445125.1	A	7123	2332	1299	1416	2075
FJ445126.1	A	7131	2354	1292	1414	2069	FJ445127.1	A	7133	2375	1287	1408	2062
FJ445128.1	A	7133	2336	1347	1429	2019	FJ445129.1	A	7138	2380	1311	1391	2056
FJ445130.1	B	7223	2405	1423	1405	1989	FJ445131.1	A	7129	2397	1275	1436	2019
FJ445132.1	A	7114	2352	1406	1424	1932	FJ445133.1	A	7132	2342	1275	1439	2074
FJ445134.1	A	7109	2360	1364	1404	1981	FJ445135.1	A	7118	2371	1328	1395	2022
FJ445136.1	A	7152	2349	1350	1425	2025	FJ445137.1	B	7216	2334	1517	1473	1891
FJ445138.1	A	7134	2353	1326	1418	2036	FJ445139.1	A	7133	2364	1327	1413	2029
FJ445140.1	A	7136	2342	1323	1381	2088	FJ445141.1	A	7134	2414	1287	1401	2031
FJ445142.1	A	7140	2233	1363	1415	2128	FJ445143.1	A	7139	2390	1315	1391	2042
FJ445144.1	A	7139	2340	1361	1416	2022	FJ445145.1	A	7131	2371	1270	1391	2095
FJ445146.1	A	7141	2320	1352	1411	2058	FJ445147.1	A	7162	2353	1383	1429	1997
FJ445148.1	A	7139	2390	1339	1393	2016	FJ445149.1	A	7135	2377	1325	1435	1998
FJ445151.1	B	7211	2316	1499	1504	1890	FJ445152.1	A	7161	2375	1362	1427	1997
FJ445153.1	B	7216	2372	1461	1452	1931	FJ445154.1	A	7136	2368	1281	1406	2077
FJ445155.1	B	7224	2369	1421	1433	2001	FJ445156.1	A	7138	2389	1341	1421	1984
FJ445157.1	A	7116	2357	1339	1406	2011	FJ445158.1	A	7116	2336	1333	1434	2013
FJ445159.1	A	7116	2331	1334	1437	2014	FJ445160.1	A	7123	2325	1325	1454	2019
FJ445161.1	B	7230	2382	1376	1460	2011	FJ445162.1	B	7201	2392	1420	1410	1977
FJ445163.1	A	7140	2355	1334	1412	2039	FJ445164.1	B	7213	2388	1374	1420	2028
FJ445165.1	A	7150	2235	1388	1416	2111	FJ445166.1	A	7152	2227	1387	1425	2113
FJ445167.1	A	7124	2394	1295	1409	2025	FJ445168.1	B	7221	2376	1515	1450	1878
FJ445169.1	B	7233	2338	1430	1463	2002	FJ445170.1	A	7110	2371	1382	1413	1944
FJ445171.1	A	7134	2316	1344	1446	2026	FJ445172.1	B	7207	2403	1410	1418	1975
FJ445173.1	A	7133	2387	1299	1381	2066	FJ445174.1	B	7208	2404	1400	1384	2018
FJ445175.1	A	7140	2319	1317	1433	2071	FJ445176.1	A	7146	2284	1339	1382	2140
FJ445177.1	A	7132	2347	1309	1449	2021	FJ445178.1	A	7137	2331	1369	1420	2017
FJ445179.1	A	7093	2318	1336	1417	2022	FJ445180.1	A	7136	2387	1314	1425	2010
FJ445181.1	A	7129	2333	1379	1441	1972	FJ445182.1	A	7128	2334	1347	1420	2027
FJ445183.1	A	7145	2356	1379	1429	1981	FJ445184.1	A	7152	2241	1381	1406	2121
FJ445185.1	A	7132	2344	1384	1444	1957	FJ445186.1	B	7217	2377	1401	1447	1992
FJ445187.1	B	7224	2372	1411	1466	1971	FJ445188.1	B	7216	2322	1497	1490	1907
FJ445189.1	A	7119	2370	1328	1408	2011	FJ445190.1	A	7132	2392	1307	1389	2044
L05355.1	B	7212	2313	1460	1475	1964	L24917.1	A	7124	2383	1331	1412	1998
V01149.1	HEV	7440	2206	1737	1711	1786	X02316.1	A	7102	2324	1347	1418	2013

Table S12: Accession, group, sequence length of coronavirus data

Accession	Group	Length	N_A	N_C	N_G	N_T
AF304460.1	Group 1	27317	7420	4549	5903	9445
AF353511.1	Group 1	28033	6937	5382	6397	9317
NC_005831.2	Group 1	27553	7253	3979	5516	10805
AY391777.1	Group 2	30738	8485	4658	6655	10940
U00735.2	Group 2	31032	8490	4713	6774	11055
AF391542.1	Group 2	31028	8486	4743	6772	11027
AF220295.1	Group 2	31100	8544	4711	6790	11055
NC_003045.1	Group 2	31028	8487	4752	6767	11022
AF208067.1	Group 2	31233	8087	5591	7466	10089
AF201929.1	Group 2	31276	8117	5548	7422	10189
AF208066.1	Group 2	31112	8030	5534	7416	10132
NC_001846.1	Group 2	31357	8138	5614	7487	10118
NC_001451.1	Group 3	27608	7967	4479	5993	9169
EU095850.1	Group 3	27657	7969	4513	6066	9108
AY278488.2	Group 4	29725	8465	5941	6185	9134
AY278741.1	Group 4	29727	8455	5940	6188	9144
AY278491.2	Group 4	29742	8475	5942	6183	9142
AY278554.2	Group 4	29736	8476	5942	6185	9133
AY282752.2	Group 4	29736	8476	5939	6185	9136
AY283794.1	Group 4	29711	8453	5937	6184	9137
AY283795.1	Group 4	29705	8447	5936	6187	9135
AY283796.1	Group 4	29711	8453	5936	6185	9137
AY283797.1	Group 4	29706	8451	5935	6184	9135
AY283798.2	Group 4	29711	8453	5935	6185	9138
AY291451.1	Group 4	29729	8457	5940	6188	9144
NC_004718.3	Group 4	29751	8481	5940	6187	9143
AY297028.1	Group 4	29715	8458	5934	6187	9135
AY572034.1	Group 4	29540	8402	5911	6154	9073
AY572035.1	Group 4	29518	8395	5907	6151	9065
NC_006577.2	Group 5	29926	8331	3895	5699	12001
NC_001564.2	Flaviviridae outgroup	10682	2618	2531	2919	2614
NC_004102.1	Flaviviridae outgroup	9646	1889	2893	2724	2140
NC_001512.1	Togaviridae outgroup	11835	3676	2860	2859	2440
NC_001544.1	Togaviridae outgroup	11657	3220	2901	3065	2416

Table S13: Accession, group, sequence length of influenza A virus data

Accession	Group	Length	N_A	N_C	N_G	N_T
HM370969.1	H1N1	1419	453	263	330	373
CY138562.1	H1N1	1422	437	259	343	383
CY149630.1	H1N1	1433	441	261	346	385
KC608160.1	H1N1	1398	409	251	357	381
AM157358.1	H1N1	1413	418	259	355	381
AB470663.1	H1N1	1422	418	252	359	393
AB546159.1	H1N1	1410	421	260	351	378
HQ897966.1	H1N1	1410	422	246	353	389
EU026046.2	H1N1	1433	439	263	347	384
FJ357114.1	H1N1	1433	438	253	350	392
GQ411894.1	H1N1	1413	430	260	346	376
CY140047.1	H1N1	1433	440	261	347	385
KM244078.1	H1N1	1410	447	261	335	367
HQ185381.1	H5N1	1350	406	240	339	365
HQ185383.1	H5N1	1350	408	240	336	366
EU635875.1	H5N1	1350	397	248	347	358
FM177121.1	H5N1	1370	407	245	350	368
AM914017.1	H5N1	1350	398	243	344	365
KF572435.1	H5N1	1350	403	247	345	355
AF509102.2	H5N1	1366	401	257	344	364
AB684161.1	H5N1	1350	404	235	348	363
EF541464.1	H5N1	1350	396	246	349	359
JF699677.1	H5N1	1350	404	236	348	362
GU186511.1	H5N1	1370	407	244	345	374
EU500854.1	H7N3	1453	475	284	339	355
CY129336.1	H7N3	1428	470	278	332	348
CY076231.1	H7N3	1420	467	286	327	340
CY039321.1	H7N3	1434	470	288	333	343
AY646080.1	H7N3	1453	485	284	329	355
KF259734.1	H7N9	1398	478	290	321	309
KF938945.1	H7N9	1404	483	287	322	312
KF259688.1	H7N9	1413	490	291	320	312
KC609801.1	H7N9	1426	488	292	332	314
CY014788.1	H7N9	1460	500	306	337	317
CY186004.1	H7N9	1422	494	303	317	308
DQ017487.1	H2N2	1467	445	281	355	386
CY005540.1	H2N2	1467	455	284	344	384
JX081142.1	H2N2	1457	446	265	349	397

Table S14: Accession, group, sequence length of bacteria 16S rDNA data

Accession	Family	Length	N_A	N_C	N_G	N_T
KY486204.1	Methylobacteriaceae	1104	263	265	345	230
KY486205.1	Xanthomonadaceae	761	194	165	256	146
KY486206.1	Xanthomonadaceae	1452	361	340	464	287
KY486207.1	Intrasporangiaceae	1253	301	295	395	262
KY486218.1	Microbacteriaceae	1195	296	286	372	241
KY486219.1	Pseudomonadaceae	1099	282	250	339	228
KY927407.1	Bacillaceae	718	179	179	206	154
KY486220.1	Paenibacillaceae	1335	327	326	419	263
KY486221.1	Enterobacteriaceae	1339	335	314	430	260
KY486222.1	Xanthomonadaceae	1337	335	313	422	267
KY486223.1	Microbacteriaceae	1334	317	314	435	268
KY486209.1	Rhodanobacteraceae	1366	332	319	447	268
KY486210.1	Enterobacteriaceae	1356	338	324	431	262
KY486232.1	Enterobacteriaceae	1350	337	318	432	262
KY019246.1	Enterobacteriaceae	1346	335	318	431	262
KY013009.1	Enterobacteriaceae	1351	337	318	434	262
KY927404.1	Microbacteriaceae	742	184	177	232	149
KY486211.1	Enterobacteriaceae	1365	337	325	441	262
KY013011.1	Staphylococcaceae	1035	278	226	299	231
KY019245.1	Enterobacteriaceae	1344	334	317	430	262
KY013010.1	Bacillaceae	1343	336	318	420	269
KY486208.1	Enterobacteriaceae	1269	318	298	400	253
KY486212.1	Microbacteriaceae	1364	341	324	436	263
KY486213.1	Xanthomonadaceae	1387	345	322	442	278
KY486228.1	Enterobacteriaceae	1356	337	325	429	265
KY486224.1	Enterobacteriaceae	1346	335	317	431	262
KY486225.1	Enterobacteriaceae	1294	329	312	401	251
KY486226.1	Enterobacteriaceae	1347	338	316	432	261
KY927405.1	Enterobacteriaceae	753	189	169	252	143
KY486227.1	Enterobacteriaceae	1345	336	317	431	261
KY927408.1	Microbacteriaceae	785	193	188	243	161
KY486214.1	Enterobacteriaceae	1411	352	330	455	274
KY927406.1	Microbacteriaceae	796	201	183	266	146
KY486215.1	Enterobacteriaceae	1319	338	309	417	255
KY486216.1	Enterobacteriaceae	1345	335	317	430	263
KY486217.1	Enterobacteriaceae	1341	335	315	431	260
KY486229.1	Enterobacteriaceae	1345	335	318	432	260
KY486230.1	Pseudomonadaceae	1346	345	306	416	279
KY486231.1	Enterobacteriaceae	1322	325	321	419	255
KY019244.1	Enterobacteriaceae	1337	331	315	428	260

Table S15: Accession, group, sequence length of bacteria data

Accession	Family	Length	N_A	N_C	N_G	N_T
CP001598.1	Bacillaceae	5227419	1685408	930043	919269	1692699
AE016879.1	Bacillaceae	5227293	1685374	930007	919244	1692668
CP001215.1	Bacillaceae	5230115	1667671	974191	876267	1711986
AE017225.1	Bacillaceae	5228663	1685622	930391	919481	1693169
CP000976.1	Borreliaceae	931674	335148	129225	127787	339514
CP000048.1	Borreliaceae	922307	321202	137556	137547	326002
CP000993.1	Borreliaceae	930981	335785	129350	126839	339007
CP000049.1	Borreliaceae	917330	322493	133424	133693	327720
CP000246.1	Clostridiaceae	3256683	1148078	470943	453276	1184386
CP000312.1	Clostridiaceae	2897393	1017083	423439	395046	1061825
BA000016.3	Clostridiaceae	3031430	1060154	446732	419228	1105316
CP000527.1	Desulfovibrionaceae	3462887	639427	1092219	1089813	641428
AE017285.1	Desulfovibrionaceae	3570858	659017	1127624	1127109	657108
CP002297.1	Desulfovibrionaceae	3532052	652227	1113805	1116142	649878
AM260480.1	Burkholderiaceae	2912490	486037	972789	972298	481366
CP000091.1	Burkholderiaceae	2726152	480326	883953	887595	474278
CP000578.1	Rhodobacteraceae	1219053	192966	416292	420323	189472
CP001151.1	Rhodobacteraceae	1297647	204455	445520	446045	201627
AM295250.1	Staphylococcaceae	2566424	833636	449856	438966	843965
AE015929.1	Staphylococcaceae	2499279	837991	405441	396707	859140
AP006716.1	Staphylococcaceae	2685015	907537	437414	443072	896992
CP001837.1	Staphylococcaceae	2658366	878689	445972	454367	879338
AL590842.1	Yersiniaceae	4653728	1219520	1102670	1114185	1217353
CP001585.1	Yersiniaceae	4640720	1216182	1097565	1112625	1214348
AE009952.1	Yersiniaceae	4600755	1200303	1090469	1101384	1208599
CP001593.1	Yersiniaceae	4553586	1187961	1077463	1093635	1194527
CP001671.1	Enterobacteriaceae	5131397	1271011	1298314	1297349	1264723
CP000468.1	Enterobacteriaceae	5082025	1256126	1285309	1283517	1256945
CP001383.1	Enterobacteriaceae	4650856	1145625	1187110	1177854	1140266
AE005674.2	Enterobacteriaceae	4607202	1133784	1176618	1167963	1128831

References

- [1] Masatoshi Nei. Phylogenetic analysis in molecular evolutionary genetics. *Annual review of genetics*, 30(1):371–403, 1996.
- [2] Matthew I Bellgard, Takeshi Itoh, Hidemi Watanabe, Tadashi Imanishi, and Takashi Gojobori. Dynamic evolution of genomes and the concept of genome space. *Annals of the New York Academy of Sciences*, 870(1):293–300, 1999.
- [3] Fabian Sievers, Andreas Wilm, David Dineen, Toby J Gibson, Kevin Karplus, Weizhong Li, Rodrigo Lopez, Hamish McWilliam, Michael Remmert, Johannes Söding, et al. Fast, scalable generation of high-quality protein multiple sequence alignments using clustal omega. *Molecular systems biology*, 7(1):539, 2011.
- [4] Kazutaka Katoh and Daron M Standley. Mafft multiple sequence alignment software version 7: improvements in performance and usability. *Molecular biology and evolution*, 30(4):772–780, 2013.

- [5] Robert C Edgar. Muscle: multiple sequence alignment with high accuracy and high throughput. *Nucleic acids research*, 32(5):1792–1797, 2004.
- [6] Yuta Hozumi, Rui Wang, Changchuan Yin, and Guo-Wei Wei. Umap-assisted k-means clustering of large-scale sars-cov-2 mutation datasets. *Computers in biology and medicine*, 131:104264, 2021.
- [7] Jiahui Chen and Guo-Wei Wei. Omicron ba. 2 (b. 1.1. 529.2): high potential for becoming the next dominant variant. *The journal of physical chemistry letters*, 13(17):3840–3849, 2022.
- [8] Jiahui Chen, Yuchi Qiu, Rui Wang, and Guo-Wei Wei. Persistent laplacian projected omicron ba. 4 and ba. 5 to become new dominating variants. *Computers in biology and medicine*, 151:106262, 2022.
- [9] Michael Bleher, Lukas Hahn, Maximilian Neumann, Juan Angel Patino-Galindo, Mathieu Carriere, Ulrich Bauer, Raul Rabadan, and Andreas Ott. Topological data analysis identifies emerging adaptive mutations in sars-cov-2. *arXiv preprint arXiv:2106.07292*, 2021.
- [10] Juan Ángel Patiño-Galindo, Ioan Filip, Ratul Chowdhury, Costas D Maranas, Peter K Sorger, Mohammed AlQuraishi, and Raul Rabadan. Recombination and lineage-specific mutations linked to the emergence of sars-cov-2. *Genome Medicine*, 13:1–14, 2021.
- [11] Susana Vinga. Alignment-free methods in computational biology, 2014.
- [12] Andrzej Zielezinski, Susana Vinga, Jonas Almeida, and Wojciech M Karlowski. Alignment-free sequence comparison: benefits, applications, and tools. *Genome biology*, 18:1–17, 2017.
- [13] Oliver Bonham-Carter, Joe Steele, and Dhundy Bastola. Alignment-free genetic sequence comparisons: a review of recent approaches by word analysis. *Briefings in bioinformatics*, 15(6):890–905, 2014.
- [14] Guillaume Bernard, Cheong Xin Chan, and Mark A Ragan. Alignment-free microbial phylogenomics under scenarios of sequence divergence, genome rearrangement and lateral genetic transfer. *Scientific reports*, 6(1):28970, 2016.
- [15] Andrzej Zielezinski, Hani Z Girgis, Guillaume Bernard, Chris-Andre Leimeister, Kujin Tang, Thomas Dencker, Anna Katharina Lau, Sophie Röhling, Jae Jin Choi, Michael S Waterman, et al. Benchmarking of alignment-free sequence comparison methods. *Genome biology*, 20:1–18, 2019.
- [16] Se-Ran Jun, Gregory E Sims, Guohong A Wu, and Sung-Hou Kim. Whole-proteome phylogeny of prokaryotes by feature frequency profiles: An alignment-free method with optimal feature resolution. *Proceedings of the National Academy of Sciences*, 107(1):133–138, 2010.
- [17] Gregory E Sims, Se-Ran Jun, Guohong Albert Wu, and Sung-Hou Kim. Whole-genome phylogeny of mammals: evolutionary information in genic and nongenic regions. *Proceedings of the National Academy of Sciences*, 106(40):17077–17082, 2009.
- [18] B Edwin Blaisdell. A measure of the similarity of sets of sequences not requiring sequence alignment. *Proceedings of the National Academy of Sciences*, 83(14):5155–5159, 1986.
- [19] Tiejie Wu, John P Burke, and Daniel B Davison. A measure of dna sequence dissimilarity based on mahalanobis distance between frequencies of words. *Biometrics*, pages 1431–1439, 1997.
- [20] Tiejie Wu, Ya-Ching Hsieh, and Lung-An Li. Statistical measures of dna sequence dissimilarity under markov chain models of base composition. *Biometrics*, 57(2):441–448, 2001.
- [21] Tiejie Wu, Ying-Hsueh Huang, and Lung-An Li. Optimal word sizes for dissimilarity measures and estimation of the degree of dissimilarity between dna sequences. *Bioinformatics*, 21(22):4125–4132, 2005.

- [22] Ian F Korf and Alan B Rose. Applying word-based algorithms: the imeter. *Plant Systems Biology*, pages 287–301, 2009.
- [23] Ming Li, Paul Vitányi, et al. *An introduction to Kolmogorov complexity and its applications*, volume 3. Springer, 2008.
- [24] Hasan H Otu and Khalid Sayood. A new sequence distance measure for phylogenetic tree construction. *Bioinformatics*, 19(16):2122–2130, 2003.
- [25] Myron Tribus and Edward C McIrvine. Energy and information. *Scientific American*, 225(3):179–190, 1971.
- [26] Susana Vinga and Jonas Almeida. Alignment-free sequence comparison—a review. *Bioinformatics*, 19(4):513–523, 2003.
- [27] Chenglong Yu, Troy Hernandez, Hui Zheng, Shek-Chung Yau, Hsin-Hsiung Huang, Rong Lucy He, Jie Yang, and Stephen S-T Yau. Real time classification of viruses in 12 dimensions. *PloS one*, 8(5):e64328, 2013.
- [28] Mo Deng, Chenglong Yu, Qian Liang, Rong L He, and Stephen S-T Yau. A novel method of characterizing genetic sequences: genome space with biological distance and applications. *PloS one*, 6(3):e17293, 2011.
- [29] H Joel Jeffrey. Chaos game representation of gene structure. *Nucleic acids research*, 18(8):2163–2170, 1990.
- [30] Milan Randić, Marjana Novič, and Dejan Plavšić. Milestones in graphical bioinformatics. *International Journal of Quantum Chemistry*, 113(22):2413–2446, 2013.
- [31] Pradeep Kumar Burma, Alok Raj, Jayant K Deb, and Samir K Brahmachari. Genome analysis: a new approach for visualization of sequence organization in genomes. *Journal of biosciences*, 17:395–411, 1992.
- [32] Jonas S Almeida, Joao A Carrico, Antonio Marezek, Peter A Noble, and Madilyn Fletcher. Analysis of genomic sequences by chaos game representation. *Bioinformatics*, 17(5):429–437, 2001.
- [33] Patrick J Deschavanne, Alain Giron, Joseph Vilain, Guillaume Fagot, and Bernard Fertil. Genomic signature: characterization and classification of species assessed by chaos game representation of sequences. *Molecular biology and evolution*, 16(10):1391–1399, 1999.
- [34] Bai-Lin Hao. Fractals from genomes—exact solutions of a biology-inspired problem. *Physica A: Statistical Mechanics and its Applications*, 282(1-2):225–246, 2000.
- [35] Tung Hoang, Changchuan Yin, Hui Zheng, Chenglong Yu, Rong Lucy He, and Stephen S-T Yau. A new method to cluster dna sequences using fourier power spectrum. *Journal of theoretical biology*, 372:135–145, 2015.
- [36] Changchuan Yin, Ying Chen, and Stephen S-T Yau. A measure of dna sequence similarity by fourier transform with applications on hierarchical clustering. *Journal of theoretical biology*, 359:18–28, 2014.
- [37] Ajay Kumar Saw, Garima Raj, Manashi Das, Narayan Chandra Talukdar, Binod Chandra Tripathy, and Soumyadeep Nandi. Alignment-free method for dna sequence clustering using fuzzy integral similarity. *Scientific reports*, 9(1):3753, 2019.
- [38] Chenglong Yu, Qian Liang, Changchuan Yin, Rong L He, and Stephen S-T Yau. A novel construction of genome space with biological geometry. *DNA research*, 17(3):155–168, 2010.

- [39] Pek Y Lum, Gurjeet Singh, Alan Lehman, Tigran Ishkanov, Mikael Vejdemo-Johansson, Muthu Alagappan, John Carlsson, and Gunnar Carlsson. Extracting insights from the shape of complex data using topology. *Scientific reports*, 3(1):1236, 2013.
- [40] Joseph Minhow Chan, Gunnar Carlsson, and Raul Rabadan. Topology of viral evolution. *Proceedings of the National Academy of Sciences*, 110(46):18566–18571, 2013.
- [41] Dong Quan Ngoc Nguyen, Phuong Dong Tan Le, Lin Xing, and Lizhen Lin. A topological characterization of dna sequences based on chaos geometry and persistent homology. In *2022 International Conference on Computational Science and Computational Intelligence (CSCI)*, pages 1591–1597. IEEE, 2022.
- [42] Rui Wang, Duc Duy Nguyen, and Guo-Wei Wei. Persistent spectral graph. *International journal for numerical methods in biomedical engineering*, 36(9):e3376, 2020.
- [43] Jiahui Chen, Rundong Zhao, Yiyong Tong, and Guo-Wei Wei. Evolutionary de rham-hodge method. *Discrete and continuous dynamical systems. Series B*, 26(7):3785, 2021.
- [44] Nan Sun, Shaojun Pei, Lily He, Changchuan Yin, Rong Lucy He, and Stephen S-T Yau. Geometric construction of viral genome space and its applications. *Computational and Structural Biotechnology Journal*, 19:4226–4234, 2021.
- [45] Gregory E Sims, Se-Ran Jun, Guohong A Wu, and Sung-Hou Kim. Alignment-free genome comparison with feature frequency profiles (ffp) and optimal resolutions. *Proceedings of the National Academy of Sciences*, 106(8):2677–2682, 2009.
- [46] Ji Qi, Bin Wang, and Bai-Iin Hao. Whole proteome prokaryote phylogeny without sequence alignment: Ak-string composition approach. *Journal of molecular evolution*, 58:1–11, 2004.
- [47] Ye-Fan Hu, Terrence Tsz-Tai Yuen, Hua-Rui Gong, Bingjie Hu, Jing-Chu Hu, Xuan-Sheng Lin, Li Rong, Coco Luyao Zhou, Lin-Lei Chen, Xiaolei Wang, et al. Rational design of a booster vaccine against covid-19 based on antigenic distance. *Cell Host & Microbe*, 31(8):1301–1316, 2023.
- [48] Gunnar Carlsson. Topology and data. *Bulletin of the American Mathematical Society*, 46(2):255–308, 2009.
- [49] Herbert Edelsbrunner, John Harer, et al. Persistent homology—a survey. *Contemporary mathematics*, 453(26):257–282, 2008.
- [50] Zixuan Cang and Guo-Wei Wei. Topologynet: Topology based deep convolutional and multi-task neural networks for biomolecular property predictions. *PLoS computational biology*, 13(7):e1005690, 2017.
- [51] Duc Duy Nguyen, Zixuan Cang, Kedi Wu, Menglun Wang, Yin Cao, and Guo-Wei Wei. Mathematical deep learning for pose and binding affinity prediction and ranking in d3r grand challenges. *Journal of computer-aided molecular design*, 33:71–82, 2019.
- [52] Duc Duy Nguyen, Kaifu Gao, Menglun Wang, and Guo-Wei Wei. Mathdl: mathematical deep learning for d3r grand challenge 4. *Journal of computer-aided molecular design*, 34:131–147, 2020.
- [53] Facundo Mémoli, Zhengchao Wan, and Yusu Wang. Persistent laplacians: Properties, algorithms and implications. *SIAM Journal on Mathematics of Data Science*, 4(2):858–884, 2022.
- [54] Jian Liu, Jingyan Li, and Jie Wu. The algebraic stability for persistent laplacians. *arXiv preprint arXiv:2302.03902*, 2023.
- [55] Rui Wang, Rundong Zhao, Emily Ribando-Gros, Jiahui Chen, Yiyong Tong, and Guo-Wei Wei. Hermes: Persistent spectral graph software. *Foundations of data science (Springfield, Mo.)*, 3(1):67, 2021.

- [56] Xiaoqi Wei and Guo-Wei Wei. Persistent sheaf laplacians. *Foundations of data science (Springfield, Mo.)*, doi:10.3934/fods.2024033, 2024.
- [57] Rui Wang and Guo-Wei Wei. Persistent path laplacian. *Foundations of data science (Springfield, Mo.)*, 5(1):26, 2023.
- [58] Dong Chen, Jian Liu, Jie Wu, and Guo-Wei Wei. Persistent hyperdigraph homology and persistent hyperdigraph laplacians. *Foundations of Data Science*, 5(4):558–588, 2023.
- [59] Yuchi Qiu and Guo-Wei Wei. Persistent spectral theory-guided protein engineering. *Nature computational science*, 3(2):149–163, 2023.
- [60] Zhenyu Meng and Kelin Xia. Persistent spectral-based machine learning (perspect ml) for protein-ligand binding affinity prediction. *Science advances*, 7(19):eabc5329, 2021.
- [61] Yuta Hozumi and Guo-Wei Wei. Analyzing single cell rna sequencing with topological nonnegative matrix factorization. *Journal of Computational and Applied Mathematics*, page 115842, 2024.
- [62] Sean Cottrell, Rui Wang, and Guo-Wei Wei. Plpca: Persistent laplacian-enhanced pca for microarray data analysis. *Journal of Chemical Information and Modeling*, 2023.
- [63] Hongyu Yu and Stephen S-T Yau. The optimal metric for viral genome space. *Computational and Structural Biotechnology Journal*, 23:2083–2096, 2024.
- [64] Danuta M Skowronski, Catharine Chambers, Gaston De Serres, Suzana Sabaiduc, Anne-Luise Winter, James A Dickinson, Jonathan B Gubbay, Kevin Fonseca, Steven J Drews, Hugues Charest, et al. Serial vaccination and the antigenic distance hypothesis: effects on influenza vaccine effectiveness during a (h3n2) epidemics in canada, 2010–2011 to 2014–2015. *The Journal of infectious diseases*, 215(7):1059–1099, 2017.
- [65] Tyler N Starr, Allison J Greaney, Sarah K Hilton, Daniel Ellis, Katharine HD Crawford, Adam S Dingens, Mary Jane Navarro, John E Bowen, M Alejandra Tortorici, Alexandra C Walls, et al. Deep mutational scanning of sars-cov-2 receptor binding domain reveals constraints on folding and ace2 binding. *cell*, 182(5):1295–1310, 2020.
- [66] Jiahui Chen, Daniel R Woldring, Faqing Huang, Xuefei Huang, and Guo-Wei Wei. Topological deep learning based deep mutational scanning. *Computers in Biology and Medicine*, 164:107258, 2023.
- [67] JunJie Wee and Guo-Wei Wei. Rapid response to fast viral evolution using alphafold 3-assisted topological deep learning. *arXiv preprint arXiv:2411.12370*, 2024.
- [68] Ivica Letunic and Peer Bork. Interactive tree of life (itol) v6: recent updates to the phylogenetic tree display and annotation tool. *Nucleic Acids Research*, page gkae268, 2024.